DEVELOPMENT OF AMINO FUNCTIONALIZED POSS BASED (3-GLYCIDOXYPROPYL)TRIMETHOXYSILANE HYBDRID SOL-GEL COATINGS FOR AIRCRAFT APPLICATIONS

A THESIS SUBMITTED TO
THE GRADUATE SCHOOL OF NATURAL AND APPLIED SCIENCES
OF
MIDDLE EAST TECHNICAL UNIVERSITY

BY

DİLARA ÇİSEL VARAN

IN PARTIAL FULFILLMENT OF THE REQUIREMENTS
FOR
THE DEGREE OF MASTER OF SCIENCE
IN
METALLURGICAL AND MATERIALS ENGINEERING

DECEMBER 2021

Approval of the thesis:

DEVELOPMENT OF AMINO FUNCTIONALIZED POSS BASED (3-GLYCIDOXYPROPYL)TRIMETHOXYSILANE HYBDRID SOL-GEL COATINGS FOR AIRCRAFT APPLICATIONS

submitted by **DİLARA ÇİSEL VARAN** in partial fulfillment of the requirements for the degree of **Master of Science** i**n Metallurgical and Materials Engineering, Middle East Technical University** by,

Prof. Dr. Halil Kalıpçılar
Dean, Graduate School of **Natural and Applied Sciences** _____

Prof. Dr. C. Hakan Gür
Head of the Department, **Met. and Materials Eng., METU** _____

Prof. Dr. Abdullah Öztürk
Supervisor, **Met. and Materials Eng., METU** _____

Examining Committee Members:

Prof. Dr. Hüsnü Emrah Ünalan
Metallurgical and Materials Eng., METU _____

Prof. Dr. Abdullah Öztürk
Metallurgical and Materials Eng., METU _____

Prof. Dr. Çekdar Vakıf Ahmetoğlu
Materials Science and Eng., İYTE _____

Assoc. Prof. Dr. Batur Ercan
Metallurgical and Materials Eng., METU _____

Assist. Prof. Dr. Simge Çınar Aygün
Metallurgical and Materials Eng., METU _____

Date: 08.12.2021

I hereby declare that all information in this document has been obtained and presented in accordance with academic rules and ethical conduct. I also declare that, as required by these rules and conduct, I have fully cited and referenced all material and results that are not original to this work.

Name, Last name : Dilara Çisel Varan

Signature :

ABSTRACT

DEVELOPMENT OF AMINO FUNCTIONALIZED POSS BASED (3-GLYCIDOXYPROPYL)TRIMETHOXYSILANE HYBDRID SOL-GEL COATINGS FOR AIRCRAFT APPLICATIONS

Varan, Dilara Çisel
Master of Science, Metallurgical and Materials Engineering
Supervisor: Prof. Dr. Abdullah Öztürk

December 2021, 86 pages

An amino functionalized and 50 percent amphiphilic polyhedral oligomeric silsesquioxane (POSS) based (3-Glycidoxypropyl)trimethoxysilane (GPTMS) sol-gel reaction was carried out under extreme basic conditions. Amount of POSS per 1 mol of GPTMS was varied at molar ratios of 0.2, 0.4, and 0.6. The sol-gel product was coated on the aluminium 2024 alloy samples with immersion technique and thermally treated to improve corrosion resistance of the alloy. Influence of aging durations (1, 3, and 6 days) on the sol-gel reactions and polymerization of the coating layer were investigated using Fourier Transform Infrared (FTIR) spectroscopy. Thermal properties of the cured samples were analyzed by Differential Scanning Calorimetry (DSC) measurements and Thermo-mechanical analyzer (TMA). Surface properties and corrosion performance of the coatings were tested using contact angle measurement and Electrochemical Impedance Spectroscopy (EIS) techniques, respectively. A 0.6 mole amino functionalized POSS incorporated, and 6 days aged GPTMS revealed better corrosion resistance and hydrophobic features.

Keywords: Hybrid Sol-gel Coating, GPTMS, Amino-POSS, Al 2024 T3.

ÖZ

HAVA ARACI UYGULAMALARI İÇİN AMİNO FONKSİYONEL POSS BAZLI (3-GLİSİDOKSİPROPİL)TRİMETOKSİSİLAN HİBRİT SOL-GEL KAPLAMALARININ GELİŞTİRİLMESİ

Varan, Dilara Çisel
Yüksek Lisans, Metalurji ve Malzeme Mühendisliği
Tez Yöneticisi: Prof. Dr. Abdullah Öztürk

Aralık 2021, 86 sayfa

Amino ile işlevselleştirilmiş ve yüzde 50'si amfifilik polihedral oligomerik silseskioksan (POSS) bazlı (3-glisidoksipropil)trimetoksisilan (GPTMS) sol-jel reaksiyonu ekstrem bazik koşullar gerçekleştirildi. 1 mol GPTMS başına POSS miktarı, 0.2, 0.4 ve 0.6'lık molar oranlarında değiştirildi. Sol-jel ürünü, alüminyum 2024 alaşım numuneleri üzerine daldırma tekniği ile kaplandı ve alaşımın korozyon direncini artırmak için ısıl işleme tabi tutuldu. Yaşlandırma sürelerinin (1, 3 ve 6 gün) sol-jel reaksiyonları ve kaplama tabakasının polimerizasyonu üzerindeki etkisi Fourier Dönüşümü Kızılötesi (FTIR) spektroskopisi kullanılarak araştırıldı. Kürlenmiş numunelerin termal özellikleri, Diferansiyel Taramalı Kalorimetri (DSC) ölçümleri ve Termo-mekanik analizör (TMA) ile analiz edildi. Kaplamaların yüzey özellikleri ve korozyon performansı sırasıyla temas açısı ölçümü ve Elektrokimyasal Empedans Spektroskopisi (EIS) teknikleri kullanılarak test edildi. 0.6 mol amino işlevselleştirilmiş POSS ilave edilmiş ve 6 gün yaşlandırılmış GPTMS, daha iyi korozyon direnci ve hidrofobik özellikler ortaya çıkardı.

Anahtar Kelimeler: Hibrit Sol-Gel Kaplama, GPTMS, Amino-POSS, Al 2024 T3.

To My Hero Mother

ACKNOWLEDGMENTS

I would like to express my deepest gratitude to my supervisor Prof. Dr. Abdullah Öztürk and Dr. Nursev Erdoğan for their guidance, advice, criticism, encouragements, and insight throughout the research.

I would also like to special thanks to Melike Tolu, Hüseyin Utkucan Kayacı, Anıl Kuban for their suggestions, comments, and valuable supports.

I would also like to thanks to Ademcan Uşak, Merve Atlıoğlu, Sema Nur Ünsal, Seda Uslu and Mürşide Yağmur Demirci for their technical works.

I would like to thank to Turkish Aerospace Industry for the economic support in the project. I am also thankful to my workmates from Prototype Manufacturing Department Tolga İşgir, İrfan İpek, Hasan Zafer Kaya, Ramazan Karakuzu, Burak Akçin, Gizem Karakelle, Bahadır Özcan, Yusuf Can Karakuş, Görkem Kanyılmaz, Suna Özkan, Bahadır Satır, Kasım Şafak Muratoğlu, Durmuş Soner Bilgin, Kübra Bolat and Orhan Faruk Şener due to motive me throughout the all research.

Moreover, special thanks should be given to Celal Onur Alkaş who encourages motivates and supports me every time.

I especially thank to my sisters, Özge Özkılınç, Yağmur Leblebicioğlu, Ezgi Özbek and Elif Fulya Mercan for their friendship and emotional support all the time.

I would like to express my gratitude to my family, Süheyla Aslan, Osman Çinel Varan, Leyla Sevim Aslan and Nejla Aslan.

Lastly, I would like to dedicate this work to my hero mother Süheyla Aslan. Many thanks with all my hearth for the most meaningful support. Everything I achieve is her work and vision.

TABLE OF CONTENTS

LIST OF TABLES

TABLES

LIST OF FIGURES

FIGURES

LIST OF ABBREVIATIONS

ABBREVIATIONS

ATR	: Attenuated Total Reflection
BSA	: Boric-Sulfuric Acid Anodizing
CAA	: Chromic Acid Anodizing
CCC	: Chemical Conversion Coating
CSA	: Chromic and Sulfuric Acids
CTE	: Coefficient of Thermal Expansion
DC	: Direct Current
DSC	: Differential Scanning Calorimetry
EIS	: Electrochemical Impedance Spectroscopy
FPL	: Forest Products Laboratory
FTIR	: Fourier Infrared Spectroscopy
GPTMS	: 3-Glycidyloxypropyl-trimethoxysilane
LP	: Linear polarization
LPR	: Linear Polarization Resistance
MEK	: Methyl-Ethyl Ketone
NMR	: Nuclear Magnetic Resonance Spectroscopy
OCP	: Open Circuit Potential

PAA : Phosphoric Acid Anodizing

PEO : Polyethylene Oxide

POSS : Polyhedral Oligomeric Silsesquioxane

PSA : Phosphoric-Sulfuric Acid Anodizing

SAA : Sulfuric Acid Anodizing

SCC : Stress Corrosion Cracking

SEM : Scanning Electron Microscopy

TEA : Triethanolamine

TEOS : Tetraethyl Orthosilicate

TEPA : Tetraethylenepentamine

TP : Tafel Extrapolation

TSA : Tartaric-Sulfuric Acid Anodizing

LIST OF SYMBOLS

SYMBOLS

ν_{as}	: Asymmetric stretching vibration
δ	: Bending mode of vibration
ρ	: Rocking mode of vibration
ν	: Stretching vibration symmetric
ν_s	: Symmetric stretching vibration
τ	: Twisting mode of vibration
ω	: Wagging mode of vibration
$\Delta E/\Delta i$	: Slope of the polarization resistance plot (μA)
βa	: Anodic tafel constants (mV)
βc	: Cathodic tafel constants (mV)
I_{CORR}	: Corrosion current (mA)
i_{CORR}	: Corrosion current density (μA/cm2)
E_{corr}	: Corrosion potential (mV)
i_{MEAS}	: Average current (μA)
$i_{O,Z}$	: Current for oxidation of Z (μA)
$i_{R,Z}$	: Current for reduction of Z+ (μA)
d	: Density of the corroding species (g/cm2)
EW	: Equivalent weight of the corroding species (g)

Tg : Glass Transition Temperature (oC)

η : Overvoltage (mV)

i_{EX} : Exchange current (μA)

CHAPTER 1

INTRODUCTION

Aluminum alloys are extensively used in automotive, aerospace, maritime industries applying several surface treatments[1] because of their desirable engineering properties such as low specific weight, good ductility, high strength and impact resistance to weight ratio, perfect electrical and thermal conductivity. However, these materials suffer from various types of corrosions for instance pitting, uniform, crevice, intergranular, galvanic, stress corrosion cracking, biological corrosion etc. during service[2]. In order to overcome this problem, a protective coating is applied onto the alloys to improve their corrosion resistance. Two types of hexavalent chromium based anodizing process; namely chemical conversion coating (CCC) and chromic acid anodizing (CAA), have been widely used in aerospace applications to achieve a protective anodic oxide film. Hexavalent (VI) chromium-based coating combines with application of primer (generally epoxy based) and, if necessary, topcoat (generally epoxy and polyurethane based) applications[3]. Anodizing process provides surface for good adhesive bonding due to self-ordered and nano porous oxide layer which the coatings with the bonded assembly provides good tensile strength and durability in harsh environmental conditions[1,4].

In spite of several advantages such as self-healing, high adhesion with aluminum materials, paints and primers, and being economically reasonable REACH (Registration, Evaluation, Authorization and Restriction of Chemicals) regulations reported in 2007 states that the use of hexavalent (VI) chromium contained hazardous chemicals will be entirely forbidden in 2024 due to their threat to both human health and environment[5]. Companies and research centers have started to research Cr (IV) free alternatives. One of the alternatives is phosphoric acid

anodizing (PAA) that was developed first by Boeing Co. in 1975. Compatibility of PAA with primer is not good as CAA although the oxide layer of PAA has more porous and thinner structure than CAA film[6]. Nowadays, research towards new anodizing techniques with different acids continue. Beside the chromate free and advantages, anodizing coating decreases fatigue strength of aluminum alloys[7]. In order to find eco-friendlier alternatives, a new trend of hybrid organic-inorganic sol-gel coatings have been studied to provide corrosion barrier against corrosive environment and good adhesion with metal substrate and organic primer-topcoat[8]. The most promising advantage of sol-gel based treatments is diversity of chemistry to have different functional properties of coating. Also sol-gel technique is cleaner, and can be performed in aqueous or any organic media which has hydrolytic or non-hydrolytic procedures, respectively[9].

Sol-gel coatings are done with organic and inorganic chemicals depending on expected function of the final coated layer. Inorganically prepared sol-gel coatings offer good adhesion layer with strong van der Waals bonds between metallic surface and polymer molecules. These bonds are transformed Me-O-Si and Al-O-Si stable covalent bonds with aluminum surface. Nevertheless, inorganically synthesized sol-gel coatings cannot provide crack free thick film since cracking is usually intervenes during drying process[10].

Hybrid sol-gel films are prepared both organically and inorganically in order to enhance film properties. Scratch resistance, durability, and good adherence to metal surfaces are enhanced by the inorganic component, while the organic component increases density, flexibility, and functional compatibility with organic paint systems, as well as the possibility of thick, crack-free coatings[11]. 3-Glycidyloxypropyl-trimethoxysilane (GPTMS) is one of the frequently applied precursor materials used as grafting agent. It facilitates synthesizing organic-inorganic materials and utilized to get anti-scratch coating, anticorrosion coating, and protective layers on organic polymers[12].

GPTMS has an epoxy ring at the end of the propyl chain. This functional group enables to achieve several chemical structures depending on the reactivity induced by different chemical surroundings. GPTMS binds easily to the organic and inorganic networks covalently as coupling agent[13]. GPTMS reacts with epoxy ring and amines which is used to fabricate curing agents of thermoset resins. However, there is a critical balance between polymerizable organic functional groups and polycondensation of the inorganic network because of the epoxy opening reactions during synthesis of GPTMS based hybrid materials. Structure of resultant material is highly dependent on catalyst types that may be acidic or basic[13].

Silsesquioxane can be classified as caged or noncaged structures. Caged silsesquioxane is called Polyhedral Oligomeric Silsesquioxane (POSS). The dimension and structure of POSS with the vertex group is 1-3 nm and highly symmetric respectively. The structural formula of POSS is (RSiO1.5)n where R is vertex groups that can be halogen, hydrogen, alkene, alkyl, aryl, arylene etc. Moreover, one or more functional groups such as methacrylate, styrene, amine, epoxy, and alcohol etc. attach to polymeric network covalently through polymerization or grafting reactions when the functional groups are introduced into POSS as vertex groups. POSS can improve physical properties of hybrid materials such as glass transition temperature, thermal stability, strength etc. with altering the molecular interactions when it is introduced into polymer chains or polymer network[14].

Jerman et al.[15] reported corrosion performance of GPTMS sol-gel on aluminum 2024-T3 substrate. T8-caged structure of tetra(3-aminopropyl)-tetraisobutyl-octasilsesquioxane (AP_4IO_4 POSS) was used as curing agent in different molar ratios of 0.125, 0.25, and 0.375, amino-POSS per 1 mol GPTMS. They concluded that 0.375 mol of amino-POSS for 1 mol of GPTMS has showed better corrosion resistance than all POSS added GPTMS, pure POSS, and pure GPTMS coatings.

The purpose of this study is to apply a 50% amphiphilic amine functionalized POSS added GPTMS coating on an Aluminum 2024-T3 alloy to increase its performance

in harsh corrosive environments. POSS was selected as amine-bearing compound. The POSS added GPTMS was prepared by the sol-gel process that was carried out under highly basic conditions. Effects of aging time on the formation of sol-gel reactions and on the coating, film cured were investigated using FTIR spectroscopy. Pre-penetrant etch was applied on Aluminum 2024-T3 substrate before coating. Coating was performed by immersion technique and subsequently cured by applying a regulated heat treatment. The corrosion performance of the coatings including different amine functionalized POSS were evaluated using electrochemical impedance spectroscopy (EIS).

CHAPTER 2

LITERATURE REVIEW

2.1 An Overview the Corrosion of 2024 T3 Aluminum Alloys

Aluminum and its alloys are significant engineering materials due to several properties such as plenty existence in earth, low specific weight, good ductility, high strength and impact resistance to weight ratio, perfect electrical and thermal conductivity[16]. Aluminum shows good corrosion resistance against neutral solution and atmospheric environments with developing thin oxide film layer. pH range of neutral solutions and atmospheric environment bring about thermodynamically stable oxide film on the material surface to prevent further corrosion. However, Aluminum is prone to corrosion with simultaneous formation of hydrogen due to dissolution of oxide layer in acidic and alkaline environments[17].

Aluminum alloys may contain different metals according to its application such as Fe, Si, Cu, Mg, Mn, and Zn. Among them, Aluminum alloys consisting Zn and Cu has better corrosion resistance. However, heat treatment of this alloy results in intergranular corrosion and stress corrosion cracking[18].

Aluminum alloys with high copper content such as 2xxx series are widely used in aerospace structural applications due to its stiffness and fatigue strength. Therefore, they are preferred especially on the skin areas of the aircraft structures. Nevertheless, this alloy is susceptible to corrosion[2]. Bare aluminum surface are metallurgically bonded (rolled onto) with high-purity aluminum surface layers to high-strength aluminum alloy core material, which is called Alclad[19]. Commonly used 2xxx series of aluminum alloy material's specifications are AMS QQ-A-250/5 and AMS QQ-A-250/4 , which have pros and cons according to mechanical, corrosion etc. properties.

The specifications also contain 2xxx series plate metallic material and sheet metal properties and their temper information. Aluminum 2024, T3 material information are presented in Table 2.1.

Table 2.1. Comparison of AMS QQ-A 250/4 and AMS QQ-A 250/5 [20,21].

Specification Info	**SAE AMS QQ-A 250/4**	**SAE AMS QQ-A 250/5**
Chemical Composition (wt%)		
Cr (0-0.1), Ti (0-0.15), Ti + Zr(0-0.2), Fe (0-0.5), Si (0-0.5), Zn (0.25), Mn (0.3-0.9), Mg(1.2-1.8), Cu (3.8-4.9), Al balanced.		
Physical Properties		
Density	2.74 g/cm³	
Melting Point	640 °C	
Thermal Expansion	23.1 x 10^{-6} /K	
Modulus of Elasticity	73 GPa	
Thermal Conductivity	121 W/m.K	
Electrical Resistivity	30 % IACS	
Mechanical Property for T3 Temper **Thickness:** Over 0.5 up to and including 3.2 mm		
Proof Strength (Min)	290	269
Tensile Strength (Min)	434	407
Elongation % (Min)	15	15

Alclad materials alone do not meet all anti-corrosion requirements such as pitting, uniform corrosion, intergranular corrosion, galvanic corrosion, crevice corrosion, erosion corrosion, stress corrosion cracking (SCC) and biological corrosion that causes material failure.

Pitting corrosion causes cavities or "holes", which is eventuated locally in the material. Al 2024-T3 materials have two intermetallic particles on the material surface, which are Al-Cu-Mg with Al_2CuMg (S Phase) nominal composition and Al-

Cu-Fe-Mn with (Cu, Mn, Fe)Al_6 more complex compositions. Especially Al_2CuMg nominal composition is mainly related to pitting corrosion of 2024-T3 alloy[22].

Heterogeneity sites of the material contain micro-flaws in the oxide film and causes potential differences between the intermetallic particles and the Al matrix. Micro-flaws in the alloy and existing galvanic couple causes the localized attack and increase pitting corrosion of Al 2024-T3 in the chloride environment[23].

Aluminum alloys resist corrosion when the material is exposed to the air or chemical attack by forming a passive film on the surface. Passive film on the surface is an oxide layer, which is stable in the pH range of 4-9 but the film is dissolved at lower and higher pH ranges. Although, the oxide film is still stable, it is not homogenous on the surface having weak points in both cases which leads to localized corrosion in the breakdown regions which is called uniform corrosion[24].

Intergranular corrosion is also a localized form of corrosion which starts with dissolution of S phase (Al_2CuMg nominal composition of Al-Cu-Mg) in the grain boundary of the material. Dissolution causes copper depleted zone along grain boundary and the attack occurs rapidly and results in the loss of strength and ductility[2].

Galvanic corrosion is also called dissimilar metal corrosion, which electrical potential differences between two dissimilar materials in a conductive solution causes to dissolving of more electrically negative material. The open circuit potential (OCP) of Al 2024 material is positive (or becomes positive after dealloying) because of intermetallic particles, which are Al_2CuMg (S-Phase). The pitting of the matrix alloy around the intermetallic particles becomes cathode and exposes galvanic corrosion[25].

Crevice corrosion is another type of localized corrosion which occurs around inaccessible gaps. Electrolyte (e.g., seawater that contains chloride ions) is trapped in these gaps and becomes stagnant. Owing to local differences in oxygen causes crevice corrosion. This form of corrosion often occurs in confined parts of

mechanical or welded assemblies such as under a bolt or around rivet heads, gaskets, and lap joints[26].

Erosion corrosion is described as enhancing corrosion rate due to mechanical force.

The deterioration on the metal surface may be aggravated when an aqueous or gaseous corrodent flows over the surface. Velocity, temperature, turbulence, presence of suspended solids affects erosion corrosion[27].

Stress corrosion cracking (SCC) is occured by residual stresses in the material under corrosive environment. Residual stresses result from faulty installation or cold deformation and forming, welding, heat treatment, machining and grinding during manufacturing. Pits on the material surface behaves like stress concentration sites and initiates stress corrosion cracking, but only corrosive environment cannot start stress corrosion cracking in the absence of stress[28].

Metabolic activities of microorganisms on the material surface cause anodic and cathodic reactions with creating electrolytic cells on the metal surface. Biological corrosion is resulted from presence of the microorganisms[29].

2.2 Anodization

Aircraft structures absolutely requires surface treatment to prevent corrosion against harsh environments. The surface treatments consist pre-treatment and adhesive bonding process. Anodization is carried out during pre-treatment stage to provide self-ordered and nano porous oxide layer which conforms with the second stage in which adhesive bonding process is performed. The second stage consists primer and topcoat application (if necessary) to provide increasing corrosion resistance, good tensile strength and durability in harsh environmental conditions and visual aesthetics and other specialized functions such as low observability[4].

Anodizing process are often categorized according to acid type used during process. Hexavalent (IV) chromium-based coating can be classified as chromate conversion

coating (CCC), where is used to need electrical conductivity and chromic acid anodizing (CAA), which have been widely used processes in aerospace, providing protective anodic oxide films for more than six decades. CAA and CCC have many advantages such as self-healing due to chromate ions, high adhesion with aluminum materials, compatibility to paints, and primers, and economically reasonable[5].

2.2.1 Hexavalent (IV) Based Anodizing

As discussed, earlier CAA is commonly used surface treatment in aerospace industry CAA consists three major steps: surface preparation, anodizing and post process. Degreasing and pickling (or etching) are done during surface preparation and between each step, the surfaces are rinsed with water properly. Then anodizing is done and finally post process are performed according to the final part requirements including primer and topcoat, which both are currently relying on Cr (VI)-based chemicals[30].

The first step is degreasing which removes oils, grease, and contamination coming from aluminum sheet manufacturing steps. Preliminary cleaning step is necessary to assure following steps. Next step is chemically removing of the modified surface layer by pickling (also called etching). Pickling can be operated in acidic or alkaline solutions. The acidic solutions are composed of mixtures of chromic and sulfuric acids (CSA) typically[31]. Pickling process has two types which are Forest Products Laboratory (FPL) and the CSA. FPL was developed in the U.S which is introduced immersing the substrate in sodium dichromate ($Na_2Cr_2O_7$) and sulfuric acid solution for 9–15 min at 65 °C. CSA is the European version of pickling process which uses lower concentrations of either chromium trioxide (CrO_3) or sodium dichromate ($Na_2Cr_2O_7$) with sulfuric acid for 30 min at 60 °C[32].

Both pickling processes follow two step reaction mechanism which the first step, hexavalent chromium catalyzes the oxidation of aluminum to alumina (Al_2O_3),

second step is dissolution of alumina in sulfuric acid following equation (1) and (2) respectively.

$$2Al + 4H_2SO_4 + Na_2Cr_2O_7 \leftrightarrow Al_2O_3 + Na_2SO_4 + Cr_2(SO_4)_3 + 4H_2O \quad (1)$$

$$Al_2O_3 + 3H_2SO_4 \leftrightarrow Al_2(SO_4)_3 + 3H_2O \quad (2)$$

Second step of the reaction is slower than the first one and at the end of the reaction, thin oxide layer is produced (represents with red line in Figure 2.1) which composed of alumina (Al_2O_3) and some minor concentrations (~0.5%) of S and Cr impurities[33].

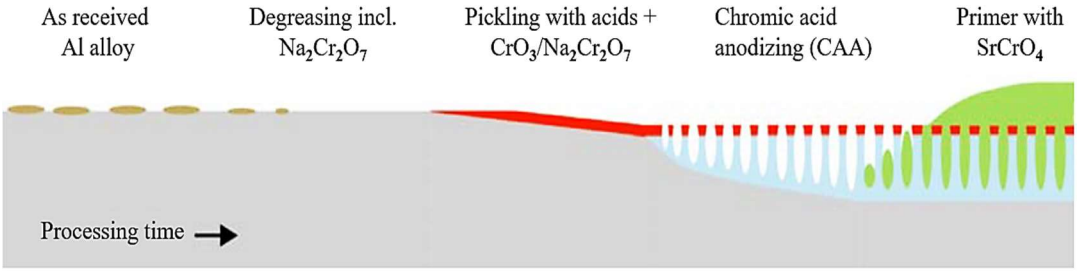

Figure 2.1. Currently used Cr-based pre-treatment in aerospace industry[31].

In the anodizing process, aluminum substrate to be treated is used as anode and Al or stainless steel is used as cathode. Electrons are withdrawn from the aluminum anode which cause the oxidation of aluminum atoms to aluminum cations (Al^{3+}) at the metal/oxide interface when the anode and the cathode are connected to the positive and negative terminal of DC power supply, respectively. Applied anodizing voltage on the anodic cell comes across a resistance by the existing oxide film which leads to a potential drop over the metal/electrolyte interface. Potential drop results in increasing electric field which enables oxide growth by ionic migration through the oxide[34]. The anode breaks down and forms negatively charged O^{-2} and OH^- anions when aluminum is anodized in an aqueous electrolyte and adsorbed water. These anions flow towards the positively charged anodic substrate and the reactions between Al^{+3} and O^{-2} leads to the formation of alumina, Al_2O_3[31,35]. The anodizing carries through barrier and porous-type oxide morphology, but porous film is needed for adhesive bonding process.

Since the 1960s, CAA has been utilized to create a thicker physical barrier between the metal and its surroundings. When the anodic oxide is soluble in the anodizing electrolyte, a porous anodic oxide layer is formed. In Europe, 40/50 V Bengough-Stuart process was adapted that using chromic acid (CrO_3) as an anodizing electrolyte. 40/50 V Bengough-Stuart process is described as a gradually increased voltage process briefly. Result in the increasing voltage in the cell produces 3–4 μm thick oxide layers on AA2024-T3 (bare and clad)[36].

Another hexavalent (IV) chromium-based coating is chemical conversion coating (CCC), which surface of metals are pre-treated both oxide and phosphate or chromate-based chemicals. The coating is used with organic coatings(primer) as a base. Also, CCC can be used without organic coating application when it works under light service conditions[30]. CCC type coating is used, where to need reflectivity, appearance, absorption, and especially, electrical resistivity and surface hardness[37].

During manufacturing operations, several hours up to several months can pass between pre-treatment and bonding operations which results in susceptible to damage, contaminations, and environmental degradation of the freshly prepared oxide[38]. The susceptibility is prevented by the application of a primer because surface activity is maximum after the pretreatment. Primer seals the oxide immediately when it is applied within two hours. Primers are described as diluted polymeric coatings which create a physical barrier between the pretreated surface and its surrounding. Primers provides chemical interaction with adhesives. So; primers have two contributing mechanisms; First one is to improve surface wetting and second one is establishing stronger chemical interactions with adhesives[39]. Improving surface wetting is provided by filling the pores completely. Coupling agents in primers provide chemical interactions with adhesives and promotes bonding the inorganic-organic interface. Coupling agents are introduced as bifunctional adhesion promoter which have the organic end groups (such as methoxy (CH_3O^-), ethoxy ($CH_3CH_2O^-$) or hydroxyl (HO^-) attach to a metallic central atom[31]. Organosilanes are coupling agents and their organic end groups can adsorb metal oxide surface via hydrogen bonds which result in forming metallosiloxane bonds

(Al–O–Si) with the surface oxide and remaining silanol groups condense and forms Si–O–Si network upon curing[40]. Durability of hydrolyzed Al-O-Si bonds depends on cross-linking of the Si–O–Si bonds which affects hydrophobicity of the covering siloxane film. Hence, chemical composition and oxide film works compatible. Franquet et al.[41] reported pre-treatment process highly affect silane film uniformity and thickness. Surface pre-treatment is needed due to increasing amount of surface hydroxyl groups if silanes are applied.

2.3 Cr(VI)- Free Anodizing Processes

2.3.1 Phosphoric Acid Anodizing (PAA)

As a first commercial alternative, phosphoric acid anodizing was introduced by Boeing in 1975. The solution for PAA consists 10 wt % phosphoric acid and anodizing occurs under applied constant voltage of 10-15 V for 25 min at 21-24 °C. The PAA oxide layer is more porous and thinner (0.5 to 2 μm) than the CAA film[3]. The film is non-hydrated $AlPO_4$ which provides higher resistivity against humidity and hot water sealing as well, which provides effective environmental stability during service[42].

The PAA process is not as good as CAA process because non compatible with chromate contained primers. Cr(VI)-based pigments inhibitors are more effective than the Cr(VI)-free alternatives, which is still in progress to obtain green inhibitor based on inorganic species (such as molybdates)[36].

2.3.2 Mixed Electrolytes Anodizing

Another most popular anodizing electrolyte is sulfuric acid which provides thicker and denser sulfuric acid anodizing (SAA) layer compared to PAA layer. SAA protective layer provides corrosion and wear resistance, even though poor adhesion. This limitation can be overcome with mixture of sulfuric acid and more aggressive

phosphoric acid in the anodizing bath, thus produced intermediate oxide structure occurs in morphological dimensions comparable to CAA[31]. The process, which is called phosphoric-sulfuric acid anodizing (PSA) was patented by Kock et al[43].

The first PSA process was described as equal amounts of sulfuric and phosphoric acids (100 g/L). This process leads phosphates on the outer layer of the oxide which provides additional resistance against hydration like PAA process[44]. Recent researches introduced new process parameters such as different amounts of phosphoric and sulfuric acids, temperature, and time periods to obtain optimal PSA conditions[45].

One of the mixed electrolyte anodizing is tartaric and sulfuric acid anodizing (TSA) which have already been reported by Kape[46] in the 1960s. The process cannot offer good permeation of adhesives into the oxide layer due to relatively low porosity in the final film. Hence, common applications of TSA process are limited to nonstructural applications. Curioni et al.[47] has been reported the role of tartaric acid as reducing the current density which causes decreasing oxide growth rate thereby the film thickness is lower than SAA at final. Contrary of lower film thickness, corrosion resistance is improved which can be explained with "buffering effect". Buffering effect can be described as remnants tartrate ions in the oxide. During TSA, tartaric acid and aluminum cations reacts with each other, then produce aluminum tartrate which have relatively low water solubility despite its high solubility in the acidic anodizing solution. During subsequent rinsing, relatively large amounts of aluminum tartrate precipitate at the pore walls due to the rapidly increased pH. Therefore, aluminum tartrate re-dissolves and produces a local buffer layer when the oxide is exposed under corrosive environment. Thus, the local buffer layer provides to limit susceptibility of localized corrosion. The corrosion resistance of TSA films can be improved by the addition of molybdate salts into the anodizing bath and by hot water sealing[46].

2.3.3 Two Step Anodizing

The better corrosion resistance and adhesion capabilities, a new type of processes was described which is TSA application after PSA resulting in a double oxide layer. (1) Another alternative process of CAA, the boric-sulfuric acid anodizing (BSA) was patented by Boeing as a similar process. (2) Considered to CAA, more uniform hexagonal arrangement and finer pores and compared to the SAA, resembled oxide structure is obtained[48]. Zhang et al.[1] reported that BSA process improves bonding and durability of structures when phosphoric acid is used as an anodizing electrolyte. However, boric acid is also known as hazardous for both environment and human health. Therefore, it may not be applicable in the future.

2.4 Sol-Gel Derived Film Coatings

As an environmentally friendly alternative of CAA, sol-gel derived coatings can be a good candidate due to its low processing temperature, application easiness and being waste free technologies. Thermal volatilization and degradation of entrapped species such as organic inhibitors are reduced when the process temperature is kept low. Liquid precursors make it easier to coat complicated shapes. Having low impurities in the final product provides waste free green coating technology [49].

The sol-gel process involves conversion of monomers in the precursor into colloidal media (sol) and integration of monomers as network (gel)[50]. Sol-gel synthesis has four main steps which are hydrolysis-condensation of the precursor, growth of the particles, gelation and drying, respectively. Reaction is initiated by hydrolysis and both hydrolysis and condensation reactions occur simultaneously. Reaction generation are affected by initial reaction conditions such as temperature, molar ratios of reactants, pH, solvent composition etc.[51].

Sol-gel coatings can be prepared inorganically or organically. Evaluation of network in inorganic coating is provided by the formation of a colloidal suspension (generally

oxides), while organic coatings' monomers are metal or metalloid alkoxide precursors M(OR)n which M is a network forming agent such as Si, Ti, Al, Zr etc.[52].

Corrosion resistance layer of inorganic sol-gel coating protects the metal substrate considerably although good properties of coating cannot achieve without cracking at low temperature because of brittle and thicker (>1μm) film properties[53]. Chou et al.[54] reported organic-inorganic hybrid sol-gel coatings to overcome the limitation of pure inorganic sol–gel coatings such as brittleness and high temperature requirement.

Hybrid sol–gel coatings have been popular due to admitting both properties of inorganically and organically prepared sol-gel coatings. Inorganic side of coatings provide thicker coating layer without cracking at lower temperature (usually < 100 °C), while organic side of the coatings can perform easily compatible with anticorrosion additive such as inhibitors and pigments[38,52].

Synthesizing OIH materials by sol–gel processes have been firstly reported by Schmidt [55] and Wilkes[56] since then siloxane based coatings for metal substrates have become rapidly an interest area in the last few decades due to their low cost and low environmental impact. Sol-gel involves both hydrolysis and condensation reactions which is the formation of an oxide network by a two-step process. The first step is hydrolysis that is followed by condensation simultaneously. During these steps, Si-OH bonds are formed and forming Si–OH group condenses with other Si–OH or Si–OR groups to form Si–O–Si (siloxane) bonds, respectively. Formed Si-OH bonds are not stable and tend to react with other species. During the formed Si–O–Si bonds, alcohol is released and provides to form a homogeneous, three-dimensional network[57].

$$Si(OR)_4 + H_2O \rightarrow Si(OH)_4 \quad \text{(Hydrolysis)} \qquad (3)$$

$$Si\text{-}OR + HO\text{-}Si \rightarrow Si\text{-}OH\text{-}Si + ROH \qquad (4)$$

$$Si\text{-}OH + HO\text{-}Si \rightarrow Si\text{-}O\text{-}Si + H_2O \qquad (5)$$

$$Si\text{-}OR + RO\text{-}Si \rightarrow Si\text{-}O\text{-}Si + R_2O \quad \text{(Condensation)} \qquad (6)$$

Accelerating the hydrolysis step of sol-gel process, acid or base catalyst are used. Jackie Ying et al.[58] have reported the effect of acid and base catalysts occur nucleophilic substitution of whereas H_2O and OH^-, respectively. Therefore, linear polymer structure is obtained in acidic conditions in which hydrolysis step occurs much more rapid than condensation. Whereas highly branched network with a ring structure is obtained under basic conditions in which condensation is accelerated as compared to hydrolysis. The reaction mechanism of both acidic and basic catalysts is shown in Figure 2.2 (a) and (b).

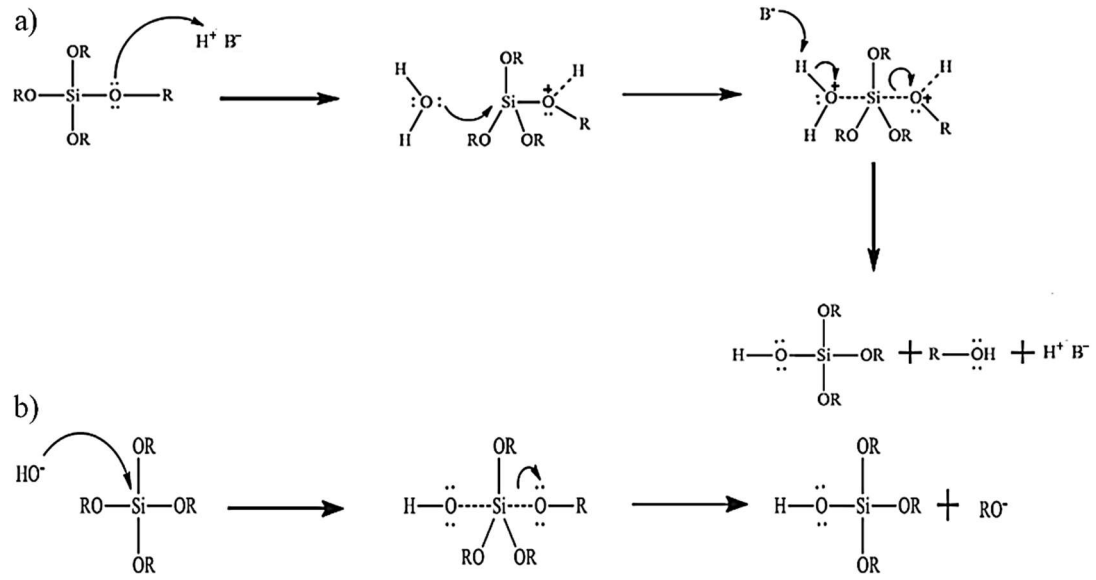

Figure 2.2. The reaction mechanism of a) acidic and b) basic conditions[59].

Final sol-gel product is mostly related to solvent type, stoichiometric amount of water added, reaction temperature and pH, where sol-gel needs to be controlled because of the nature of metal alkoxide[59].

The researchers have been focused on TEOS derived coatings and GPTMS based hybrid coatings for aluminum 2024 substrates in the last few years. TEOS sol-gel precursors are expensive and toxic to some extent despite providing better corrosion protection[8].

2.4.1 3-Glycidoxypropyltrimethoxysilane (GPTMS) Sol-Gel Film

Chemical structure of GPTMS is shown in Figure 2.3. It is widely used organically modified alkoxides to synthesize hybrid organic–inorganic materials. The applications have been reported in many different fields such as anti-scratch coatings, solid electrolytes, protective layers on organic polymers, anticorrosion coatings and restoration materials[60].

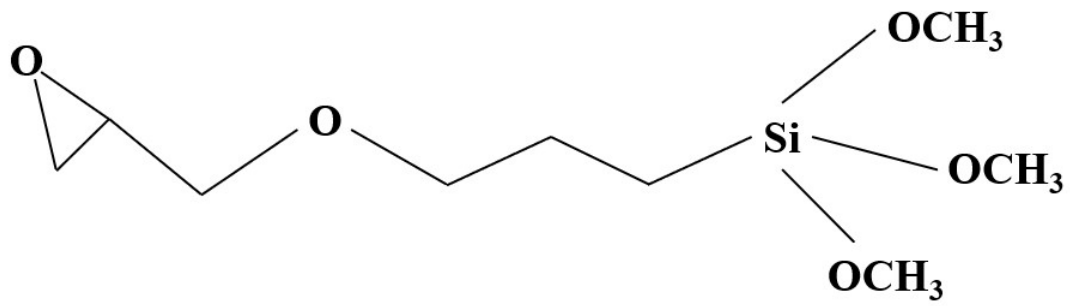

Figure 2.3. Chemical Structure of GPTMS[8].

GPTMS has a complex chemistry in which hydrolysis and condensation reactions occur simultaneously during the transition to sol-gel. In addition, making complete control of the whole process is hard to achieve due to occurred side reactions. Moreover, some changes in the chemistry of the precursor sol cause hybrid materials to have different properties and structures[61].

GPTMS has the epoxy-ring at the end of the propyl-chain that opens and allow to formation of a poly(ethylene oxide) chain under particular conditions, such as photo or thermal, basic or acidic catalysts[62]. After opening of the epoxy ring, the organic polymerization simultaneously occurs with the formation of the inorganic network. Large variety of possible reaction pathways and side reactions are possible with opened epoxy-ring. It may form both glycol units by hydrolytic ring opening and polyethylene oxide chains (PEO) of different lengths by polymerization[63].

Ingita Tiwari et al.[12] have reported possible side reactions of GPTMS sol-gel under highly basic conditions. They demonstrated the side reactions with NMR spectroscopy after epoxy opening which obtain the formation of different chemical

species: polyaddition reactions to form polyether chains, diols, dioxane rings by reaction of opened epoxies, formation of terminal methyl ether. Possible side reactions are shown in Figure 2.4.

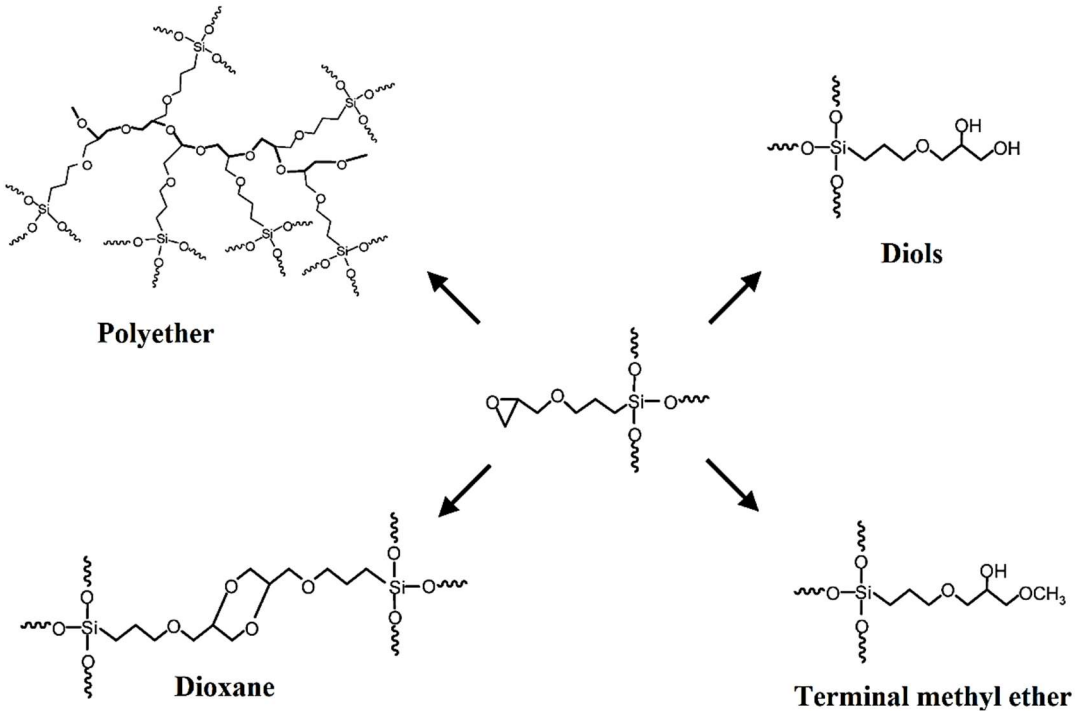

Figure 2.4. Possible side reactions of GPTMS sol-gel reaction[12].

Bouzid Menaa et al.[64] have achieved self-order, long-range organization in GPTMS sol-gel under extreme basic conditions. They proved that, increasing basicity provides the dioxane formation to link two GPTMS molecules and enhances the tendency of bridged polysilsesquioxane species. GPTMS sol-gel reaction under extreme basic conditions g are shown in Figure 2.5.

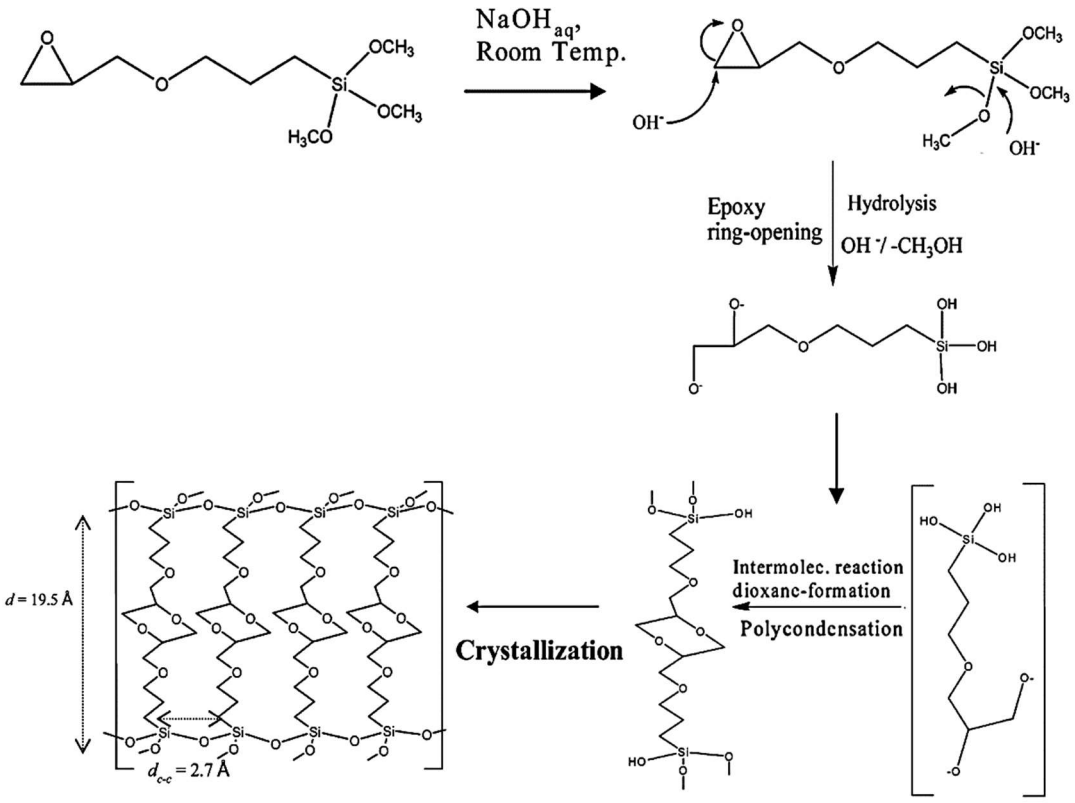

Figure 2.5. GPTMS sol-gel reaction pathway under extreme basic condition[64].

There is a relation between formation of the inorganic network and organic chain length due to forming upon opening of the epoxides. For instance, final material tends to form only oligo-species when organic moieties do not have enough time to fully polymerize due to quick forming inorganic backbone. Therefore, the properties of final material are highly related to the capability of controlling the organic and inorganic reactions.

Firstly, Gabrielli et al.[65] have demonstrated GPTMS reactivity against different pH conditions with NMR spectroscopy. Accordingly, formation of silanols and condensation are occurred immediately, then the epoxide rings are hydrolyzed and formed corresponding diols. This results in limiting the attack by the title nucleophile due to corresponding diol being the prevalent reaction and reaction needs more time to completion under highly acidic conditions (pH=2). Hydrolysis and condensation reactions are very slow at neutral pH conditions (pH=7). Hydrolysis is slow and

condensation reactions occur partially. Thus, opening of the epoxide rings does not occur because dominant process is the precipitation under basic conditions (pH=11).

Carboni et al.[66] have reported GPTMS reactivity according to the process time in different pH conditions emphasizing on the surface properties. The study suggests that lower pH conditions make surface more hydrophilic with increasing aging times. Accordingly, highly basic conditions (pH=14) allow to deposit controlled hydrophilicity. The film surface is affected by tailoring of sol aging and pH which depends on relative amount epoxides and silanols. They have also reported that higher condensation of silica network and opening of epoxide are enhanced with longer aging time which causes to decrease contact angles.

2.4.2 Amino Functionalized Curing Agents

Several chemical structures are obtained depending on the reactivity induced by different chemical surroundings due to the presence of epoxy-ring at the end of the propyl-chain. For example, fabricated a wide class of thermosetting organics or as coupling agents to covalently bind organic and inorganic networks are obtained with the reaction between the GPMTS epoxy-ring and amines which are called curing agents[13].

One of the used curing agents or nanofillers are **s**ilsesquioxane which is described the empirical formula $RSiO_{1.5}$ where R is hydrogen or any alkyl, alkylene, aryl, arylene, or organofunctional derivative of alkyl, alkylene, aryl, or arylene groups. Depending on the structure and functional groups of silsesquioxanes, properties of final materials change. Mostly synthesized silsesquioxane structures can be classified as random, ladder, cage, and partial cage[67], as shown in Figure 2.6.

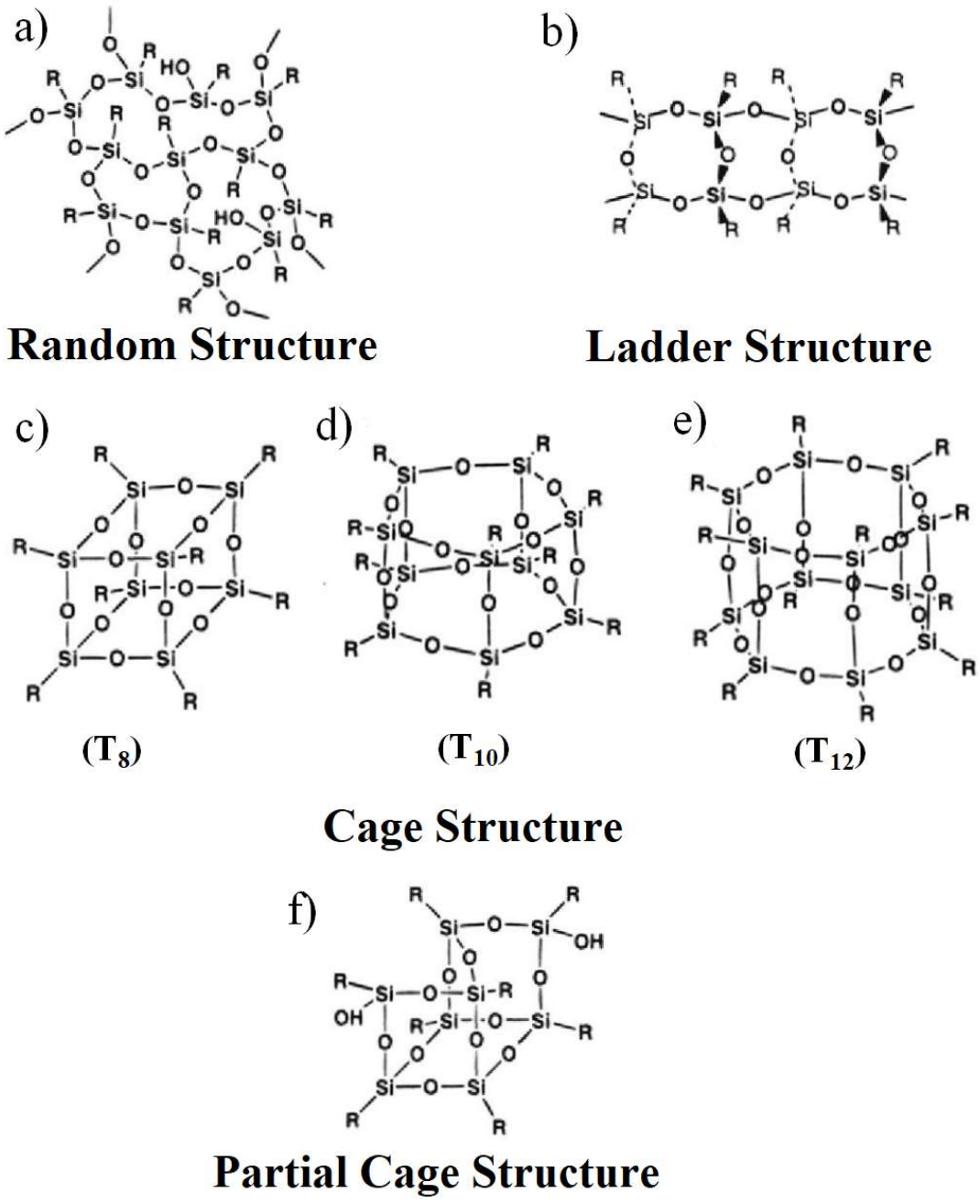

Figure 2.6. Structures of silsesquioxanes[67].

POSS is a fascinating molecule due to improving flammability resistance, surface hardness, mechanical characteristics, and oxidation resistance of polymers. Those nanofillers (size 1–3 nm) of the class of inorganic–organic materials are widely used to modify properties of many polymeric materials like thermoplastics, thermosets, and hardened polymers[68]. POSS have a cage structure and their empirical formula

can be described as $(RSiO_{1.5})n$, where R is an organic group. Depending on R group of the corner of the POSS, different substituents lead to adjustable performance which can be polar - non-polar or reactive-non-reactive[69]. Functional groups of POSS molecules can be compatible or miscible with monomers and polymers. They help to provide molecular dispersion in the resulting polymer bonding covalently with other monomers during the copolymerization or grafting onto the polymer chain or network. POSS content in nanocomposites or hybrid polymers enhances thermal and mechanical properties of final material[70,71].

On the other hand, amine compounds tend to react with the epoxy ring under catalyzed conditions[62]. GPTMS has been studied as several amines for various systems such as diethylenetriamine and triethylenetetraamine, tetraethylenepentamine (TEPA), α,ω-aminopropyl polydimethylsiloxane oligomer, ethanolamine and dimethylbenzylamine[72]. POSS molecules are functionalized with various alkyl or organic groups due to regularity of their structures[73]. POSS materials are enable to modification of thermoplastics, acrylates, polyolefins, polyurethanes, and epoxy-amine systems which have been proven to positively affect modulus of the materials, viscosity, melt flow, permeability, color and chemical resistance[68].

Amino functionalized POSS is used as an amine bearing compound to cure GPTMS, because hydrophilic amino side of POSS tends to react to opened epoxy ring of GPTMS. This tendency provides alkoxysilyl functionality and leads to further cross-linking of the polymer network. The usage of amino functionalized POSS also provides good anticorrosion properties, self-healing property and obtaining good mechanical properties[74]. The addition type of reaction between an epoxy and an amine group is shown in Figure 2.7 and Figure 2.8 with using a two-steps reaction pathway.

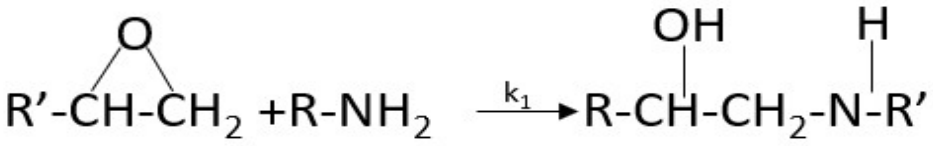

Figure 2.7. Epoxy ring opening reaction with primary amine[72].

The expressed k_1 reaction rate is higher than k_2 reaction velocity because epoxy rings are opened by a primary amine and they form a diol and a secondary amine contained compounds.

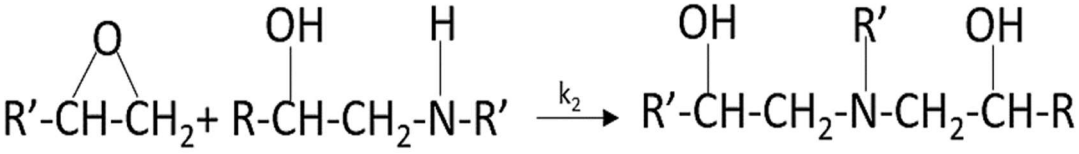

Figure 2.8. Epoxy ring opening reaction with hydrogen and secondary amine[72].

k_2 has a lower reaction rate due to slower reaction between the hydrogen and the secondary amine.

Organic substituents of POSS molecules shall be carefully selected due to influence on solubility and compatibility with a polymeric environment. Polar groups (–NCO, AcO–, –SH, –CN, $–NH_2$) provides reactivity and solubility while isobutyl, isopropyl etc. groups as a branched aliphatic substituents improve the hydrophobic property[74].

CHAPTER 3

EXPERIMENTAL PROCEDURE

3.1 Materials

Surface pre-treatment chemicals, GPTMS, amino-functionalized POSS were used without further purification. Materials used and their chemical information are presented in Table 3.1.

Table 3.1. Materials used and their chemical information.

Materials and Chemicals	Company
Aluminum 2024, T3, QQ-A-250/4 Weight percent composition: Cr (0-0.1), Ti (0-0.15), Ti + Zr (0-0.2), Fe (0-0.5), Si (0-0.5), Zn (0.25), Mn (0.3-0.9), Mg(1.2-1.8), Cu (3.8-4.9), Al balanced.	Sigma Aerospace Metals Inc.
3-Glycidyloxypropyl-trimethoxysilane (GPTMS; 98% purity)	Sigma-Aldrich Inc.
Aminopropyl-Polyhedral Oligomeric Silsesquioxane (Amino functionalized POSS, T10 Amino functionalized POSS, 50 % modified with C12 hydrophobic groups, and 50 % free amine and 50 % amide)	Funzionano AS
Bonderite C-AK4215 NC-LT AERO	Henkel Adhesive Technology
Bonderite C-IC Smut Go NC	

Table 3.1 (Cont'd.)

Methyl-Ethyl Ketone (MEK), Sodium Hydroxide powder (NaOH, 97%), Sodium Sulfide (Na_2S), Triethanolamine (TEA,99.5%), Nitric Acid(HNO_3,70%), Ethanol (EtOH, 96%)	Sigma-Aldrich Inc.
Adhesion test tape (1 inch width)	3M Company

3.2 Sample Preparation

Aluminum alloy sheets were cut with the following dimensions 500 x 500 x 1.020 mm for corrosion tests, 35 x 10 x 1.020 mm for contact angle measurements and 60 x 50 x 2.03 mm for thermo-mechanical analysis (TMA) and scanning electron microscopy (SEM). The cut samples were masked on one side not to lose electrical conductivity by using liquid and Teflon maskants. The surfaces of the aluminum samples were cleaned with MEK to remove grease, oil by hand cleaning technique with a gauze, and alkaline cleaning was completed with Bonderite C-AK4215 NC-LT AERO chemical with immersion technique for 6 min. Then, alkaline etching was applied (mixture of different concentrations of 125 g/L of NaOH, 11 g/L of Na_2S and 30 g/L of TEA chemicals) for 1 min. Acid pickling, mixture of Bonderite C-IC Smut Go NC and 50 g/L of nitric acid was applied with an immersion technique for 5 min accordingly to remove the oxide layer and intermetallic particles on the metal surface. Samples were rinsed with deionized water between all steps throughout the changing time range in 3 and 6 min. Cleaned surface was dried at 80 ^oC and 1 h in a drying oven after final rinsing to provide better adhesion with the coating. Sample surface preparation is shown in Figure 3.1.

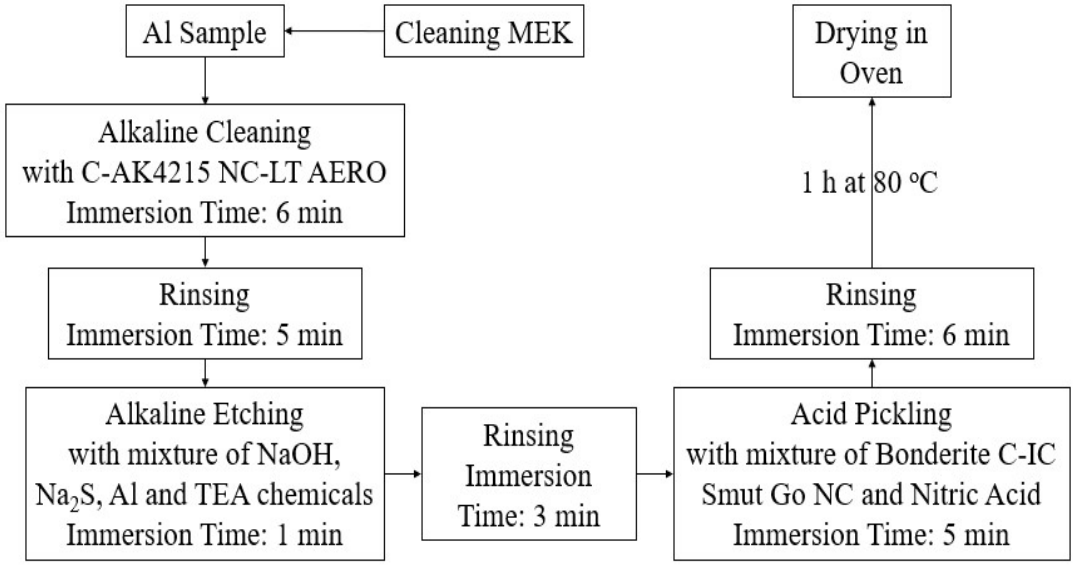

Figure 3.1. Pre-penetrant etch process of aluminum samples.

3.3 Preparation of Hybrid Sol-Gel Film Coating

Amino-POSS was received as powder form and used as a curing agent of polymerization. A 10 g of POSS was dissolved in EtOH:Water (volumetric percent of 95:5 mL) and mechanically stirred throughout a day at 70 °C. Amino functionalized POSS structure is shown in Figure 3.2.

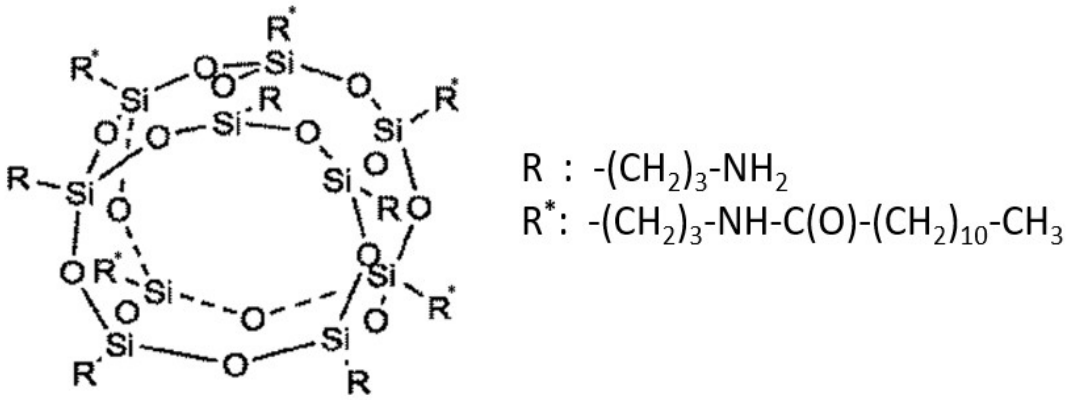

Figure 3.2. Amino functionalized POSS structure.

Hybrid silica sol was prepared under extreme basic conditions (pH:14) at room temperature by mixing of GPTMS in EtOH:Water media. The mixture of 2 mL of

GPTMS in EtOH:Water (volumetric percent of 95:5 mL) was sonicated through 30 min, with 400 W. Then 1 mL of 2 M (0.16 g of NaOH and 102.22 mmol of H_2O) NaOH was added to 100 mL of solution to catalyze the hydrolysis and the condensation reactions. After addition of catalyst, mixture was stirred mechanically 15 min at room temperature and the amino functionalized POSS was added and stirred mechanically 15 min more in a molar ratio of GPTMS:POSS = 1:0.2, 1:0.4 and 1:0.6 which were chosen because one GPTMS molecule has active species for every active H atom in NH_2 groups in amino functionalized POSS after the hydrolysis and the condensation reactions. All reactions were named and used data were given below Table 3.2 for every samples. SP00 sample was prepared for comparison purposes to understand the effect of amino functionalized POSS addition.

Table 3.2. Name of samples and description of sample preparation routes.

Sample Name	***Descriptions***
SP00	2 mL GPTMS : 5 mL DI Water : 95 mL EtOH + 1 mL NaOH
SP10	2 mL GPTMS : 5 mL DI Water : 95 mL EtOH+ 1 mL NaOH + 0.2 mol Amino functionalized POSS
SP20	2 mL GPTMS : 5 mL DI Water : 95 mL EtOH+ 1 mL NaOH + 0.4 mol Amino functionalized POSS
SP30	2 mL GPTMS : 5 mL DI Water : 95 mL EtOH+ 1 mL NaOH+0.6 mol Amino functionalized POSS

Prepared solutions were aged for 1, 3, and 6 days to obtain high reaction efficiency. The degree of ring opening, hydrolysis and the condensation reactions were determined with FTIR measurements.

3.4 Coating and Curing Process

Aluminum samples, (prepared and cleaned) in nominal dimensions of 500 x 500 x 1.020 mm, 35 x 10 x 1.020 mm, and 60 x 50 x 2.03 mm were coated with immersion coating technique for 4 min at room temperature. Preparation of samples for coating and coating procedure are shown schematically in Figure 3.3. After coating, samples were kept 1 h at room temperature before curing process. Curing was carried out with a heating rate of 5 °/min, at 120 °C. After holding 1 h at 120 °C, samples were cooled down to room temperature naturally in the cure oven. No vacuum was applied during the process. Cure cycle diagram is shown Figure 3.4. The corresponding data is tabulated in Table 3.3.

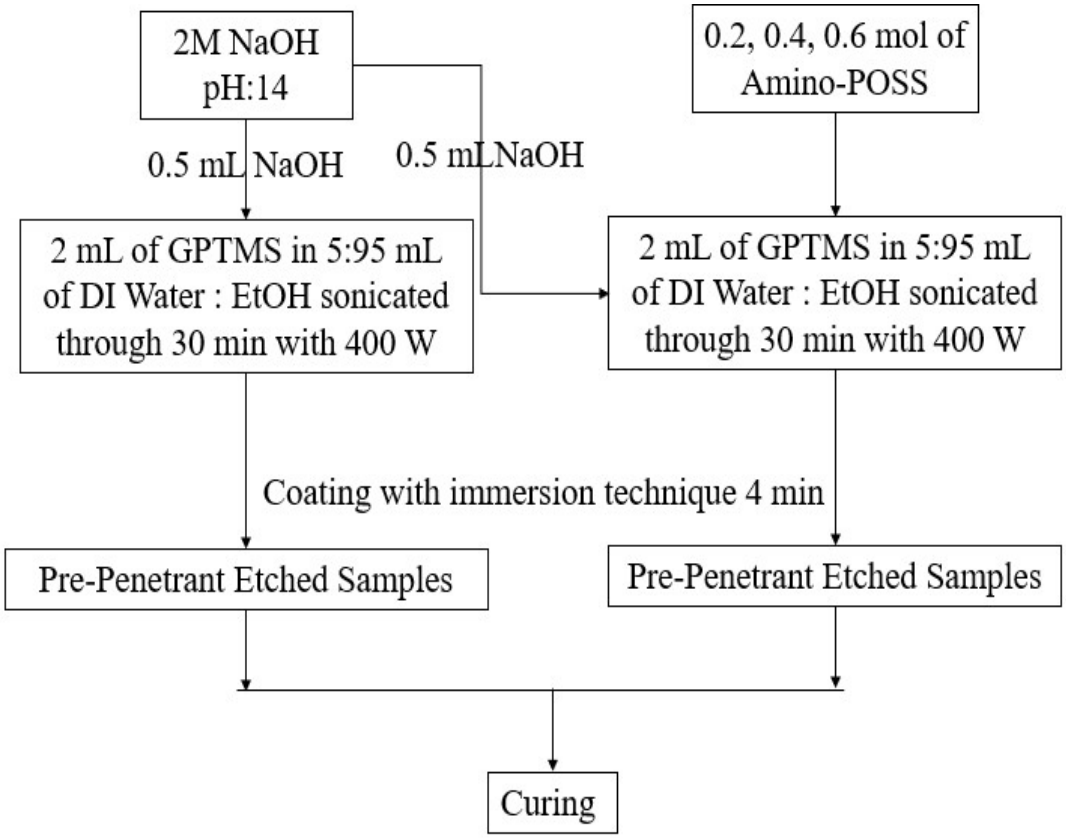

Figure 3.3. Preparation of coating and coating of samples.

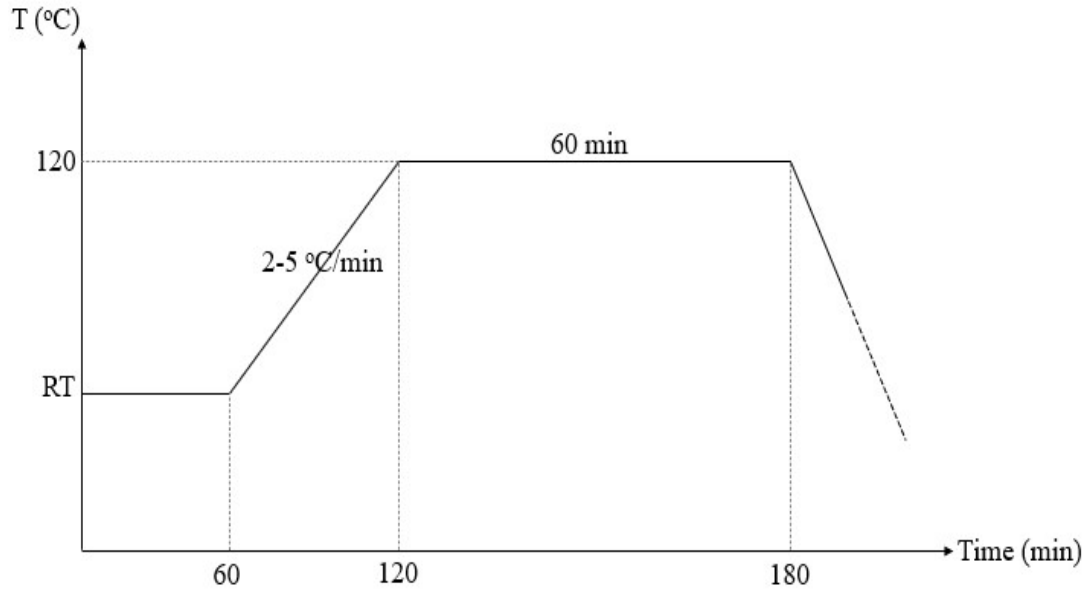

Figure 3.4. Cure cycle diagram.

Table 3.3. Cure cycle parameters.

Characteristics	**Units**	**Requirements**
Heat-up Rate	°C/min	2-5
Cure Temperature	°C	120 +/-5°
Cure Duration	min	60-(-0/+30)
Cool-down Rate	°C/min	5-7

After the curing process, the name of the samples and their descriptions are presented in Table 3.4. SP000 sample was prepared for reference.

Table 3.4. Description of sample after curing.

Sample Name	***Descriptions***
SP000	Al samples were immersed into prepared 2 mL GPTMS : 5 mL DI Water : 95 mL EtOH + 1 mL NaOH coating for 4 min and cured according to Figure 3.1

Table 3.4 (Cont'd)

SP101	Al samples were immersed into prepared 2 mL GPTMS : 5 mL DI Water : 95 mL EtOH+1 mL NaOH + 0.2 mol Amino functionalized POSS coating for 4 min and cured according to Figure 3.1
SP201	Al samples were immersed into prepared 2 mL GPTMS : 5 mL DI Water : 95 mL EtOH+1 mL NaOH + 0.4 mol Amino functionalized POSS coating for 4 min and cured according to Figure 3.1
SP301	Al samples were immersed into prepared 2 mL GPTMS : 5 mL DI Water : 95 mL EtOH+1 mL NaOH +0.6 mol Amino functionalized POSS coating for 4 min and cured according to Figure 3.1

Behaviors of aircraft working environmental conditions of the coated samples against temperature were tested by differential scanning calorimeter (DSC), and thermomechanical analysis (TMA) measurements. Adhesion test and electrochemical impedance spectroscopy (EIS) were completed to determine non-coated area on the surface and corrosion resistance of coating, respectively.

Surface topology of coated surface, hydrophobic properties of the coated surface, roughness, and thickness of coating were viewed and measured by using scanning electron microscopy (SEM), contact angle (Goniometer) measurements, surface roughness tester, and ball-ball micrometer, respectively.

3.5 Characterization Technique

3.5.1 Fourier-Transform Infrared Spectroscopy

The Fourier transform infrared (FTIR) transmission spectra of synthesized SP00, SP10, SP20, and SP30 were measured by Perkin Elmer Frontier instrument. Scans were completed on KBr pellet in the range of wavelength of 600 to 4000 cm^{-1} which were based on 16 runs through 1, 3, and 6 days. Polymerization of the coated and cured samples were measured with FTIR- Attenuated Total Reflection (ATR) apparatus in the range of 600 – 4000 cm^{-1} with a resolution of 1 cm^{-1}. The coated surface was torqued 90 N.m with diamond bit apparatus of ATR during measurements. A linear baseline was fitted to the IR spectra then normalized to signal intensity.

3.5.2 Differential Scanning Calorimeter Measurement

Cure cycle of SP00, SP10, SP20, and SP30 samples was simulated by using differential scanning calorimeter (DSC) measurements, according to EN6041 standard. A 10 mg of coating samples in liquid form was put in hermetic close pan and heated from 20 ºC to 130 ºC at 5 ºC/min heating rate.

DSC measurements of the samples cured for coating were completed by using hermetic open pan according to EN6064 standard. A 10 mg cured powder samples SP000, SP101, SP201, and SP301 were cooled until -50 ºC under nitrogen gas. Samples were heated from -50 ºC to 130 ºC at 10 ºC/min heating rate. Both experiments were realized with TA Instrument device and the results were analyzed by TA Universal Analysis program.

3.5.3 Adhesion Test

Aluminum samples with nominal dimensions of 500 x 500 x 1.020 mm were crosscut according to NEN-EN-ISO 2409 standard. The shape of crosscut was consisted of 6 square grids with nominal dimensions of 2 x 2 mm. A 25.4 mm width of adhesive test tape was pasted on the crosscut samples by a roller. Then, the tape was pulled with 60° angle, and whether the non-coated places on squares were checked. Crosscut and pulling procedure of the test are shown in Figure 3.5. This test results were evaluated according to NEN-EN-ISO 2409-Class 0.

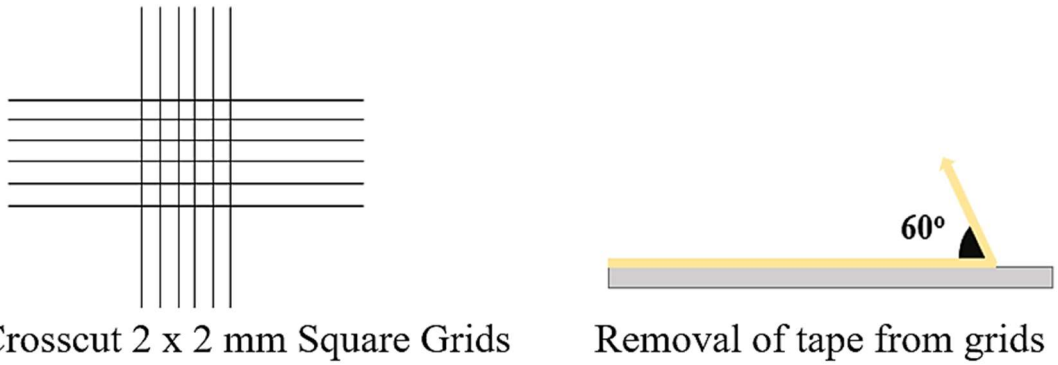

Figure 3.5. Application procedure of adhesion test.

Surface images of the adhesion test applied samples were taken by HUVITZ optical microscopy to view detached squares on the grid.

3.5.4 Thermomechanical Analysis (TMA)

Thermomechanical analysis (TMA) measurements were completed by using TA Instrument Discovery Series TMA 450 EM Device. 60 x 50 x 2.03 mm aluminum samples were cooled down -50 °C by nitrogen and heated to 130 °C. Coefficient of thermal expansion of the samples were measured according to ASTM E 831 standard. Coefficient of thermal expansion (CTE) was calculated using Eq.1.

$$\alpha = \frac{\Delta L}{L * \Delta T} \quad \text{(Eq.1)}$$

α: Coefficient of thermal expansion

ΔL: Fractional change in length

ΔT: Fractional change in temperature

3.5.5 Contact Angle Measurements

Contact angle measurements were completed by using Attension Measurement Device. Measurements were carried out as three runs and 60 x 50 x 1.020 mm aluminum samples were used which contact angle of samples were measured according to ASTM D7334 standard.

3.5.6 Surface Morphology Analysis

After coating and curing process, samples surfaces were examined by using a scanning electron microscope (SEM, JSM-6400 Electron microscope, equipped with NORAN System 6 X-Ray Microanalysis System & Semofore Digitizer). Before SEM examinations sample surfaces were coated with a thin layer of a gold-palladium alloy by a sputtering with Hummle VII Sputter Coating Device (Anatech). The spot size was changed between 3.5 or 5 while operation voltage was adjusted 10 kV during imaging depending on the sample conditions.

3.5.7 Thickness and Roughness Measurements

Roughness of as supplied aluminum sample cleaned aluminum sample and coated samples (SP000, SP101, SP201, and SP301) were measured by Mitutoyo SJ-210 roughness measurement device according to ASME B46.1 standard. Device probe was set with known roughness value plate which is 178-601 Mitutoyo plate is

2.97 Ra then measurements were completed 3 different points and values were averaged. Descriptions of aluminum reference samples are tabulated in Table 3.5.

Table 3.5. Descriptions of aluminum reference samples.

Sample Name	***Descriptions***
AL000	Al 2024, T3 samples was cleaned with MEK
ALY00	Al 2024, T3 samples was cleaned with MEK as hand cleaning then alkaline cleaning, alkaline etching and acid pickling were applied respectively.
ALC00	Al 2024, T3 samples was cleaned with MEK as hand cleaning then alkaline cleaning, alkaline etching and acid pickling were applied respectively. Then, chemical conversion coating was performed.

Thickness measurements of the coated samples were completed with ball-ball micrometer. The measurements were taken at 5 different points on the 500 x 500 x 1.020 mm substrates as shown in Figure 3.6. The data points were determined by taking the mean average of 5 measurements.

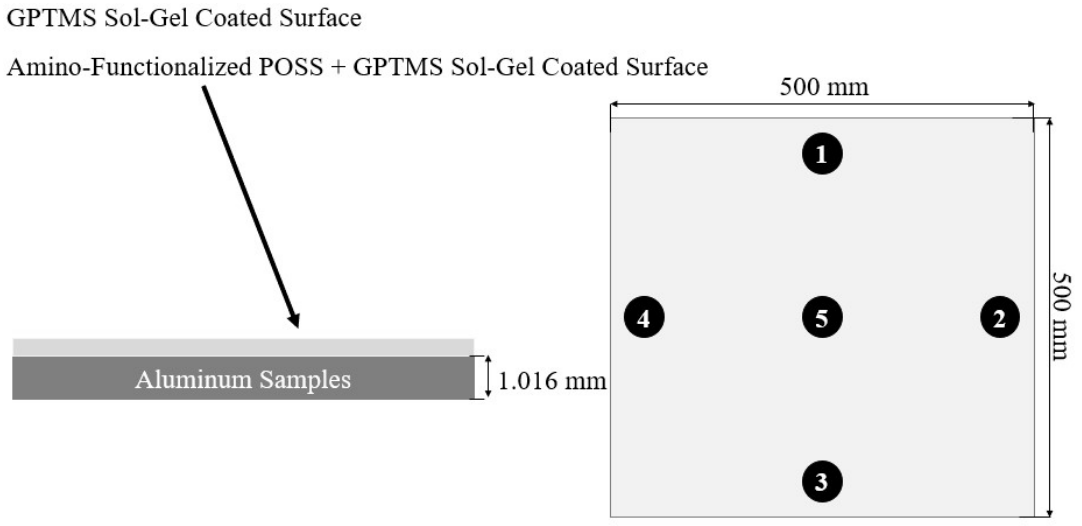

Figure 3.6. Thickness measurement of the coated samples.

3.5.8 Electrochemical Impedance Spectroscopy Measurements

Tafel curves were tested with linear polarization and electrochemical impedance spectroscopy (EIS) study. The EIS test was performed at in the range ± 10 mV, by scanning the frequencies of 100 kHz – 20 mHz. Tafel curves were plotted in the range of ± 0.25V and with a 10 mV/min velocity. Linear polarization (LP) was achieved in the range ± 0.03V at 10 mV/min velocity. Experiment parameters and conditions are presented in Table 3.6 and circuit models of coated and non-coated surface are illustrated in Figure 3.7.

Table 3.6. Experiment conditions of EIS measurements.

Plot	***Experiment Conditions***
Electrochemical Impedance Spectroscopy (EIS)	± 10 mV vs. OCV 100 kHz – 20 mHz
Tafel Extrapolation (TP)	±0.25 V vs. OCV 10 mV/min
Linear Polarization Resistance (LPR)	±0.03 V vs. OCV 10 mV/min
Experiment	
1. EIS – 1 h OCV – EIS – (10 min OCV, TP) per ASTM G59	
2. EIS – 55 min OCV – (1 min 0.03 V, LPR) per ASTM G59	

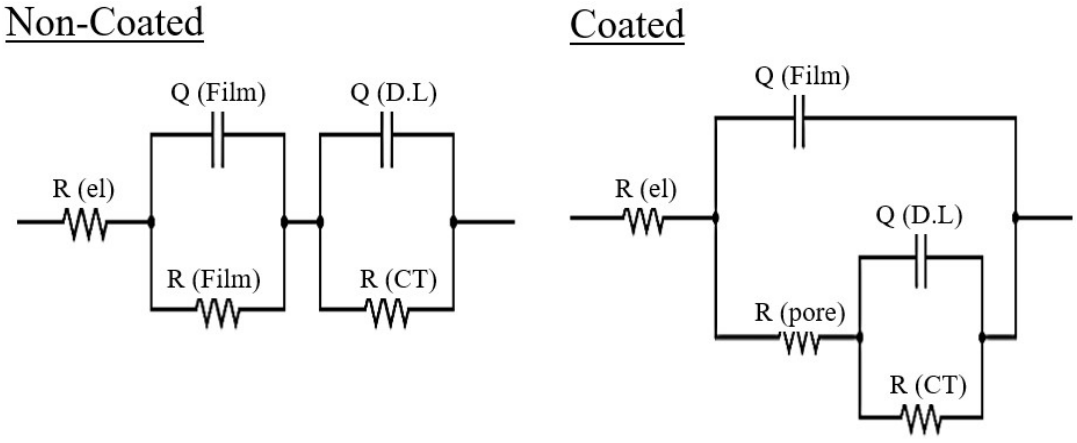

Figure 3.7. Equivalent circuit models of non-coated and coated samples.

All studies have been done at open circuit potential. Two electrochemical corrosion experiments were planned. In the first experiment, first EIS measurements were completed with explained above conditions and then the system was kept reaching open circuit potential (OCP) through 55 min. In the second EIS measurements, the system reached open circuit potential and then Tafel measurements were completed. In the second experiment, the same procedure has been applied which the system was kept reaching OCP through 55 min. After the measurements, linear polarization measurements were done as a last step, then the corrosion study continue for 48 h.

Measured data were evaluated, and the curves were plotted with using below equations.

$$i_{CORR} = \frac{\beta a\, \beta c}{2.3(\beta a + \beta c)} \frac{\Delta i}{\Delta E} \quad \text{(Eq.2)}$$

$\Delta E/\Delta i$ = slope of the polarization resistance plot (μA)

$\beta a \beta c$ = anodic and cathodic Tafel constants (mV)

$$\text{Corrosion Rate(mpy)} = \frac{0.13\ \text{Icorr(E.W)}}{d} \quad \text{(Eq.3)}$$

E.W = equivalent weight of the corroding species (g)

d = density of the corroding species (g/cm^2)

I_{CORR} = corrosion current density ($\mu A/ cm^2$)

The relation of oxidation and reduction current was considered with using the Eq.4

$$i_{MEAS} = i_{RED} - i_{OX} = 0 \quad \text{(Eq.4)}$$

The mixed potential theory was evaluated theoretically below a brief description of the derivation[75]. The non-corroding system had Z and Z^+ for example, Z was copper electrode placed into Cu^{2+} solution. The reaction below at equilibrium.

$$Z^+ + e^- \leftrightarrow Z$$

$$i_{R,Z} = i_{O,Z} = i_{EX} \quad \text{(Eq. 5)}$$

$i_{R,Z}$ = current for reduction of Z+

$i_{O,Z}$ = current for oxidation of Z

i_{EX} = the exchange current

The oxidation and reduction currents were calculated with Eq.6 and Eq.7, which presence of external voltage source:

$$i_{R,Z} = i_{EX}.e^{-\frac{\eta}{\beta'}} \quad \text{(Eq.6)}$$

$$i_{O,Z} = i_{EX}\, e^{\frac{\eta}{\beta''}} \quad \text{(Eq.7)}$$

η = overvoltage, the difference between the externally applied potential on the specimen and the corrosion potential,

$\eta = E_{APP} - E_{CORR}$

β' and β'' = constants

Taking the log of (Eq.5) and (Eq.6), which is described as Tafel equations[76], and solving for η yields:

where $\beta c = 2.3\beta'$ and $\beta a = 2.3\beta''$

CHAPTER 4

RESULTS AND DISCUSSON

4.1 Aging of GPTMS Sol-Gel Film

The epoxy ring opening of GPTMS hybrid polymer sol-gel reactions were carried out under extreme basic conditions at 1, 3, and 6 days. SP00 was used as reference for ring opening reactions, all of which were analyzed by FTIR spectroscopy. The hydrolysis and condensation reactions were examined in two different ranges: 3800-2600 cm^{-1} and 1800-600 cm^{-1} as shown in Figures 4.1-A and B. The corresponding assigned modes are presented in Table 4.1. The values and the assigned vibration modes for each absorption peak were specified using the values given in literature[77-78]. For the qualitative comparison, the spectra of 3800-2600 cm^{-1} were normalized using 2928 cm^{-1}, which is a CH_2 antisymmetric stretching band. Additionally, the 1275 cm^{-1} peak, which is a deformation of Si-CH_3 bonds, was used to normalize the 1800-600 cm^{-1} range. For the qualitative comparison, the spectra of 3800-2600 cm^{-1} were normalized using 2928 cm^{-1}, which is a CH_2 antisymmetric stretching band. Additionally, the 1275 cm^{-1} peak, which is a deformation of Si-CH_3 bonds, was used to normalize the 1800-600 cm^{-1} range. Neither of the specified peaks was invariant during polymerization[66,79]. In the present study, comparison was not carried out by increasing or decreasing the intensity of absorbance since concentration-dependent graphs may not provide accurate results during the reaction time.

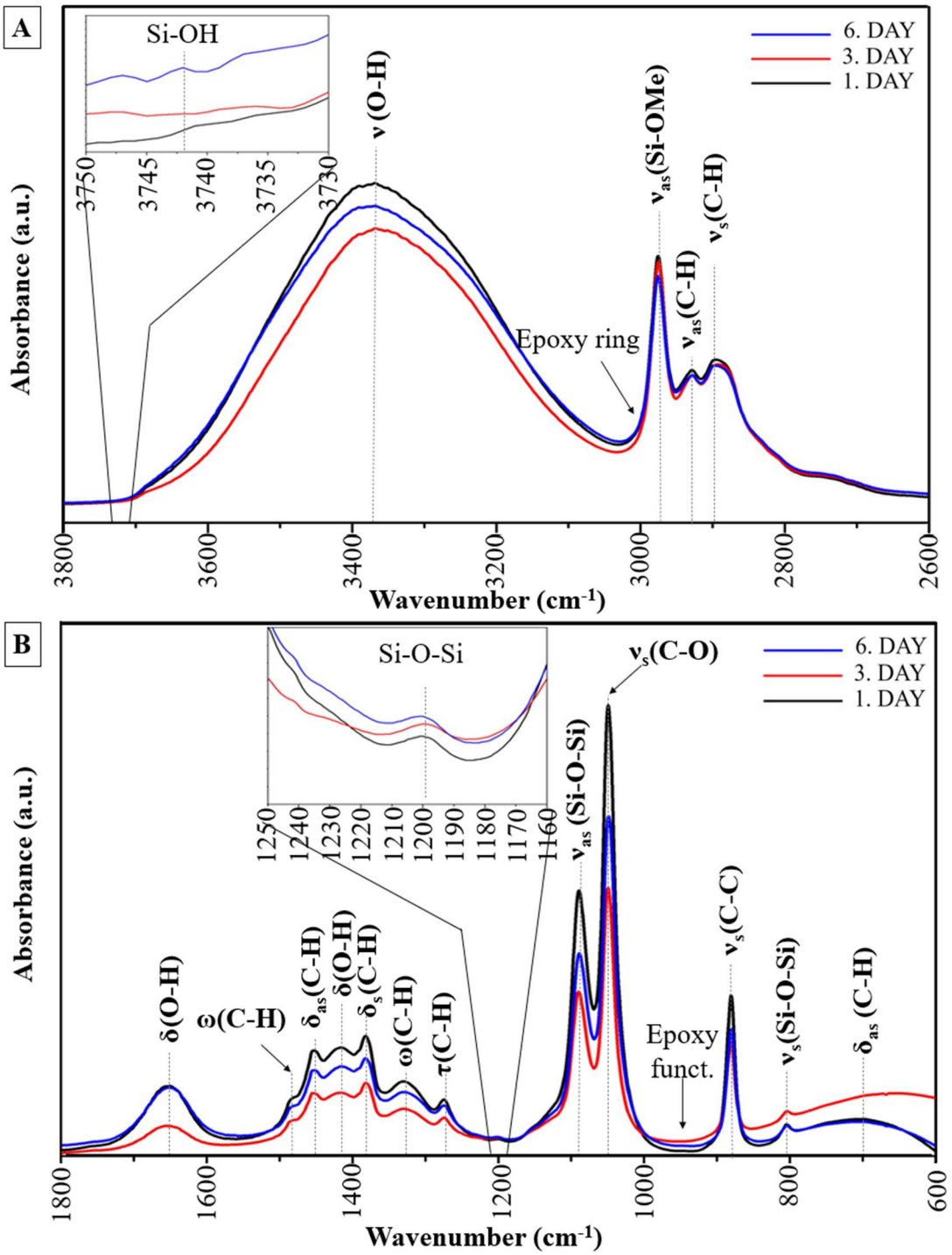

Figure 4.1. A: FTIR absorption spectra of SP00 in the range of 3800-2600 cm^{-1}, Inset spectral range: 3770-3750 cm^{-1}; B: FTIR absorption spectra of SP00 in the range of 1800-600 cm^{-1}, Inset spectral range: 1250-1160 cm^{-1}.

Table 4.1. Detected wavenumber and vibrational modes for reference sample.

Wavenumber (cm^{-1})	**Vibrational Mode**	**References**
3742	ν_{as}(Si-OH) in GPTMS	80
3389	ν (O-H)	77
2975	ν_{as}(C-H) of CH_3 in Si-OMe	77
2928	ν_{as}(C-H) of CH_2 in GPTMS	77
2895	ν_s(C-H_2) in GPTMS ν_s(C-H_3) of CH_3 in Si-OMe	77
1650	δ(O-H)	77
1474	ω(CH_3) in GPTMS	77
1452	δ_{as}(C-H) in GPTMS	77
1416	δ(O-H) of CH_2 in GPTMS	77
1382	δ_s(C-H) of CH_3 in GPTMS	77
1332	ω(C-H) of CH_2 in EtOH	77
1275	τ(C-H) of C-H in GPTMS	77
1090	ν_{as} (Si-O-Si) & ν_{as} (C-O)	77
1048	ν_{as} (Si-O-Si) & ν_s(C-O)	77
950	ν_{as}(C-O-C) in epoxy ring	81
881	ν_s(C-C) of CH_3 & CH_2 Deformation	77
805	ν_s(Si-O-Si) and ν_{as}(C-O)	78
700	δ_{as}(C-H)	77

Stretching vibration; ν, symmetric; s, asymmetric; as, bending; δ, twisting; τ, wagging; ω.

The presence of a broad peak at around 3389 cm^{-1} indicates O-H stretching vibration due to C-OH vibration of opened epoxy ring and Si-OH vibration of the remaining silanol groups. The broad region also assigns several overlap species such as water-

alcohol at ~3200 cm^{-1} and the characteristic peak of epoxy ring in the 3050-2990 cm^{-1} region[82], making it a challenge to follow up the hydrolysis and condensation reactions precisely during the aging time and using the broad band. In Figure 4.1-A, the expected peak at 3742 cm^{-1} reveals the remaining residual silanol groups on the 6. day of the aging period, indicating the formation of Si-O-Si in the hybrid matrix[80]. The presence of this formation can be confirmed by the strong peaks at 1090 cm^{-1} and 1048 cm^{-1}, which are poly(dimethylsiloxane) ($[(CH_3)_2SiO]_x$) and T units polysiloxanes $[RSiO_{1.5}]_x$. Organically modified alkoxides form quite commonly cyclic structures in highly acidic or highly basic environments, whereas cyclic and cage silica species are formed under extreme basic conditions. The cyclic species tend to reduce with the completion of the condensation of sol. A cyclic or cage structure appears at the peaks of 1036 and 1046 cm^{-1} [66]. The presence of a peak at 1048 cm^{-1} for all aging times can also be explained as the presence of a cyclic structure due to condensation of sol and polymerization of the matrix. Another characteristic peak occurs at 1198 cm^{-1}, which is an asymmetric stretching of Si-O-Si in cyclic structures shown in Figure 4.1-B. The presence of the cyclic structure is evidently confirmed by the presence of the peak. However, the peak is not enough to explain the non-completion of condensation due to several overlap species. In various condensation stages, the bond features such as distance, electronegativity, and order pertaining to Si-O in Si-O-Si are different for each condensed species. Schmidt has reported[83] that when the Si-O bond distance is constant, the vibration frequency of an asymmetric Si-O-Si in octamer and dodecamer is higher than that of the trimer and tetramer within various oligomers. The completion of polymerization in a cyclic or ring configuration species have higher dipole moments compared with an octamer or a dodecamer. However, at 1st day of aging time, the intensity of absorbance was found to be the highest among all aging days. This can be explained as a more dominant trimer and tetramer structure of sol. After heat treatment, the formation of Si-O-Si, which can also reveal the presence of polymerization, is confirmed according to the disappearance of the peak at 3742 cm^{-1}. Moreover, the detection of this peak explained the best aging time of

sol to be 6 days. The peak at 950 cm^{-1} is commonly used for ring opening and epoxy functionality in hybrid materials[80]. The peak was observed during all aging times and, upon the addition of amino-functionalized POSS, it was further followed to understand the process of reaction completion. By the addition of amino-functionalized POSS in the reaction, the active hydrogen atom in this group tended to react with the opened epoxy ring of GPTMS. Contact angle (hydrophobicity) is highly related to opened epoxy ring[63], and this makes it a crucial task to prevent possible side reactions and achieve better reaction efficiency and adhesion with aluminum samples to obtain an optimum number of opened epoxy rings. Increasing the pH level and the aging time reduces the contact angle and improves hydrophobicity[66], both of which also support the bonding tendency of amino-functionalized POSS molecules. The viscosity of the sols is a function of the aging time and increases along it. The hydrolysis, condensation and polymerization reactions lead to the alteration of viscosity due to the precursors[12]. For these reasons, the optimum aging day was chosen as 6 days. The FTIR results proved the final products of the reactions, as shown in Figure 2.5. Also, the reaction was evaluated after the heat treatment of the coating.

4.2 Aging of GPTMS Amino-Functionalized POSS Reactions

The amino-functionalized POSS in different amounts was added to the GPTMS sol-gel and aged for 1, 3, and 6 days. During the aging time, the reaction between the opened epoxy ring of GPTMS and the active hydrogen side of the amino-functionalized POSS was investigated, during which no quantitative comparisons were carried out based on the concentration-dependent graph.

For all amounts of the amino-functionalized POSS reactions with GPTMS were illustrated at two different regions in the ranges 3800-2600 cm^{-1} and 1800-600 cm^{-1}. For the qualitative comparison, the spectra of 3800-2600 cm^{-1} were normalized using 2928 cm^{-1}, which is a CH_2 antisymmetric stretching band due to invariance during polymerization[66]. The above spectra were evaluated based on

1, 3, and 6 days of aging. The 3800-2600 cm^{-1} range is shown in Figure 4.2. The detected peaks are presented in Table 4.2.

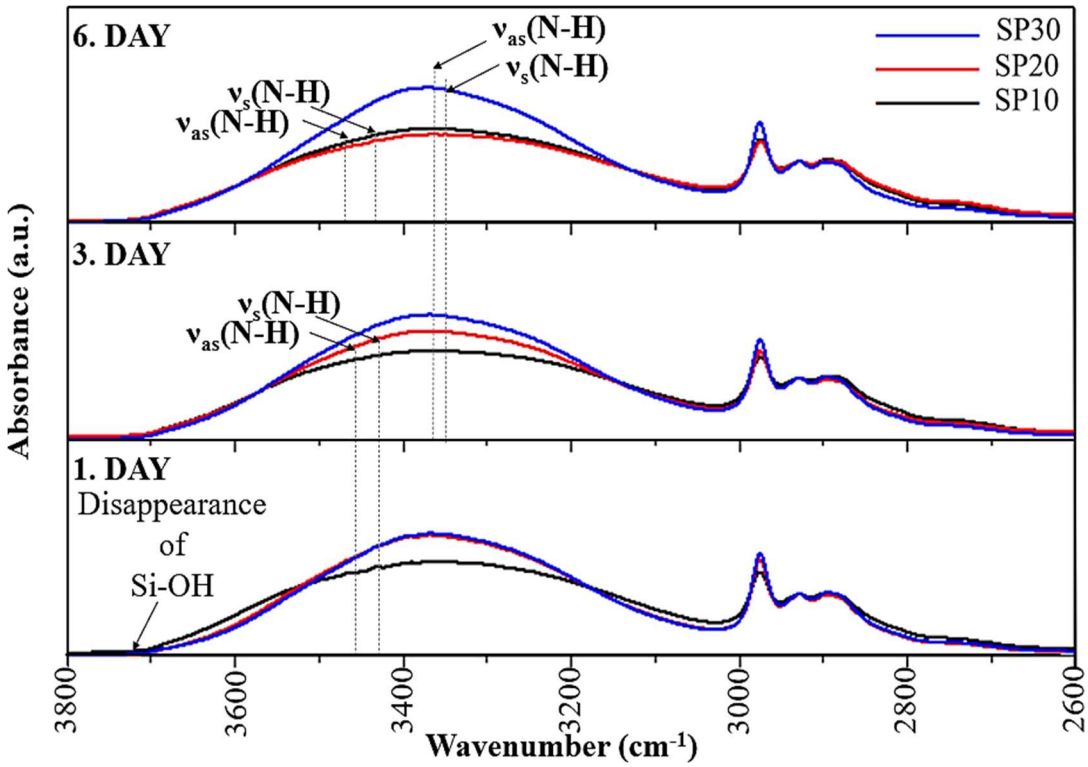

Figure 4.2. FTIR absorption spectra of SP10, SP20, and SP30 taken after 1, 3, and 6 days of aging time in the range of 3800-2600 cm^{-1}.

Table 4.2. Detected wavenumber and vibrational modes in the range 3800-2600 cm^{-1} for all amine content of GPTMS.

Wavenumber (cm^{-1})	**Vibrational Mode**	**References**
3466[84]	ν_{as}(N-H)	84
3429[85]	ν_{s}(N-H)	85
3368	ν_{as}(N-H)	85
3350	ν_{s}(N-H)	85

Stretching vibration; ν, symmetric; s, asymmetric; as.

The strong O-H stretching of hydroxyl group[86] detected at 3389 cm^{-1} for SP00 was also seen in SP10, SP20, and SP30 samples. The presence and increasing of the amine content made the peak sharper. The specified peak at 3742 cm^{-1} was not detected due to the amine content. The results show the presence of condensation reaction from 1st day. The N-H out-of-phase stretching and N-H in-phase stretching peaks were detected at 3466[84] and 3429[85] cm^{-1}, respectively, where non-bonded species disappeared on day 6 for SP10, which can be explained as the continuation of the reaction. The peaks were observed only on 1st day and 3rd day for SP20 and SP30, respectively, and disappeared at 6th day, which may be due to any non-bridge species left. The presence of an N-H stretching peak at around 3400 cm^{-1} also shows non-bonded species[87]. The peaks were observed for SP10 at the end of 6th day and only at 1st and 3rd day for SP20 and SP30. The two other band peaks at 3368 cm^{-1} and 3350 cm^{-1} were formed by the N-H in-phase stretching vibrations[85]. These peaks are assigned as hydrogen and secondary amine reaction[72], and their observation began at 3rd day for each sample because the reaction between hydrogen and secondary amine occurs at a slower rate. The epoxy ring reaction with primary amine was not observed at 6th day for SP30 sample, which may be explained as being due to the higher polymerization of the sample. The observation can be verified in the specific peak at 950 cm^{-1} in the fingerprint region.

The reaction between the opened epoxy rings and amino-functionalized POSS are investigated in several regions, namely the N-H scissoring of primary and secondary amine (at 1650-1500 cm^{-1}), the C-N stretching of aliphatic amine (at 1000-1250 cm^{-1}), and the N-H wagging of primary and secondary amine (at 910-650 cm^{-1})[88]. The 1800-600 cm^{-1} spectrum was normalized by using 1275 cm^{-1}, which is an Si-CH_3 stretching band due to invariance during the aging time[79]. No quantitative comparison was conducted due to the increasing effect of hydrolysis-condensation reaction as well as the higher amine content. However, a qualitative comparison was completed for each aging time with different amine contents as shown in Figure 4.3. The corresponding peak values are presented in Table 4.3.

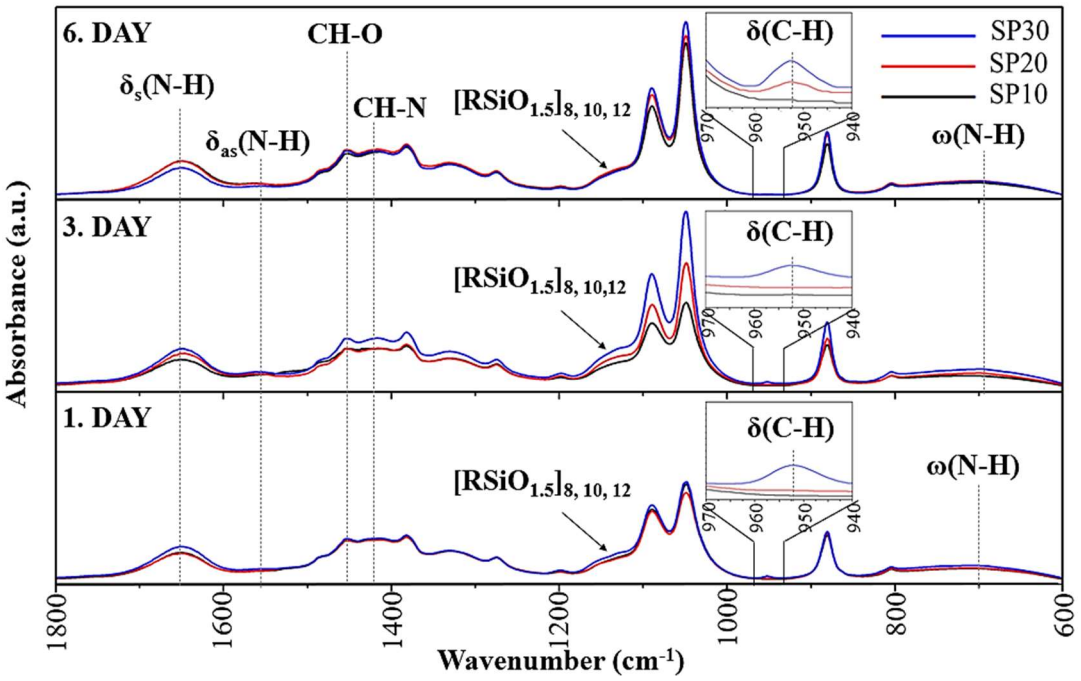

Figure 4.3. FTIR absorption spectra of SP10, SP20, and SP30, based on 1, 3, and 6 days of aging time in the range of 1800-600 cm^{-1}. Inset spectral range: 970-930 cm^{-1}.

Table 4.3. Detected wavenumber and vibrational modes in the range 800-600 cm^{-1} for all amine content of GPTMS.

Wavenumber (cm^{-1})	**Vibrational Mode**	**References**
1650	δ_s(N-H)	77
1564	δ_{as}(N-H)	89
1455	δ_s(C-H)	91
1430	δ_{as}(C-H)	91
700	ω(N-H)	77
690	ω(N-H)	90

Stretching vibration; ν, symmetric; s, asymmetric; as, bending; δ, twisting; τ, wagging; ω.

The characteristic peaks of amino-functionalized POSS can be detected in the region 1130-1115 cm^{-1} as $[RSiO_{1.5}]_{8,\ 10,\ or\ 12}$ and 1500-1650 cm^{-1} as the deformation of NH_2, respectively[89]. The peaks at 1650 and 1564 cm^{-1} were identified as being symmetric and asymmetric bending of NH_2 and overlapping with the OH bending at 1650 cm^{-1}. Another broad and characteristic peak of amine was determined at the 910-650 cm^{-1} region, which is an out-of-plane wagging of NH_2[90]. A similar wagging was seen at around 690 cm^{-1} for SP20 and SP30, and another one at around 700 cm^{-1} for SP10. The peak also shows the overlapped peak of C-H bending, and its presence may be due to a still on-going reaction at the 6^{th} day. The bonds between epoxy ring and amino-POSS can be detected by the characteristic peaks at 1455 cm^{-1} and 1430 cm^{-1} for C-O and C-N, respectively[91]. The 6^{th} day was chosen as the aging day to coat samples because the special characteristic of the epoxy ring at around 950 cm^{-1} was found at this day for SP20 and SP30. The presence of the peak for all aging times of the SP30 is explained as the increasing amount of POSS providing higher levels of polymerization. The peak assigns an out-of-plane deformation of C-H and shows a crosslinking between the epoxy ring of GPTMS and the amino-functionalized POSS[92]. It was decided that the reactions be discontinued because the viscosity of the coating tended to increase, making the aluminum surface coating impractical. As a result of the FTIR study of adding the amino-functionalized POSS, the reactions shown in Figures 2.7 and 2.8, were proved. These reactions will be evaluated after the heat treatment of the coatings.

4.3 Conformation of Cure Cycle

The cure cycle for coatings was determined by means of compiling the data available in literature[12-66-15]. Accordingly, the cure temperature was chosen as 120 ^oC at a heating rate of 5 ^{o}/min. The abundant presence of physically and chemically bounded water, adsorbed water on Si-OH and non-hydrolyzed organic moieties in the structure of the coating are all considered during the evaluation of the cure cycle[94]. Therefore, to examine the polymerization of coating, 6^{th} day-aged coating samples

were cured by differential scanning calorimetry (DSC) and using cure cycle parameters between 20 and 130 °C. During the analysis, the TA instrument program normalized the data according to the heating rate of each curve as constant at 5 °/min. The graphs taken from DSC measurements are shown in Figure 4.4. The corresponding values are presented in Table 4.4.

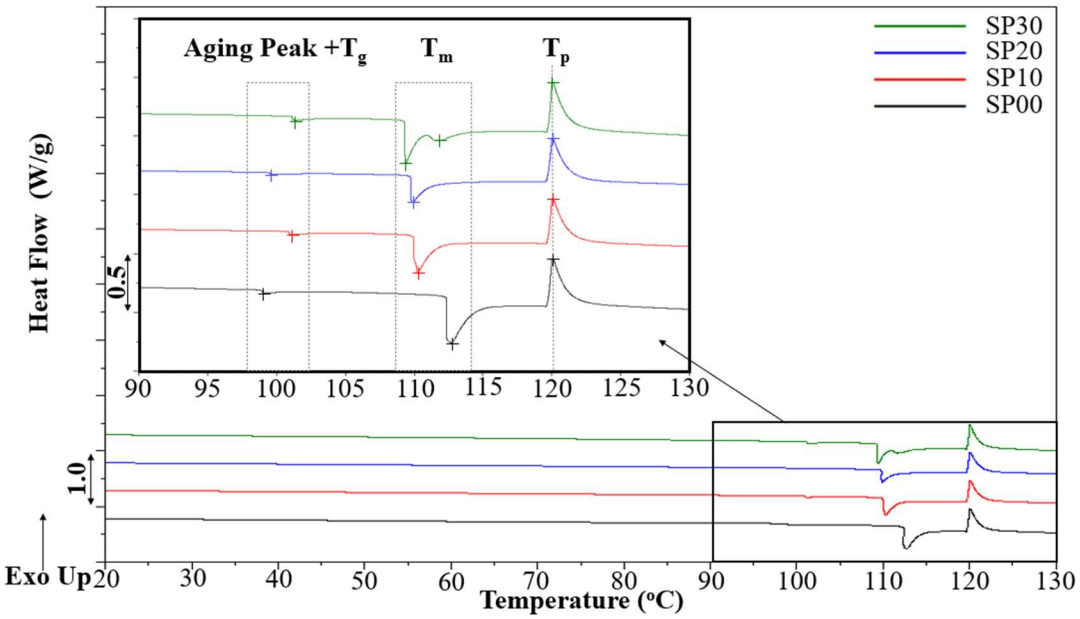

Figure 4.4. DSC measurements of SP00,SP10, SP20, and SP30 along curing duration.

Table 4.4. DSC analyses of SP00,SP10, SP20, and SP30 along curing duration.

Temperature (°C)	**SP00**	**SP10**	**SP20**	**SP30**
T_g	98.95	101.08	99.79	101.35
T_m	112.70	110.36	109.90	109.49
T_m	-	-	-	111.49
T_p	120.90	120.09	120.02	119.99

DSC analysis is carried out to measure the enthalpy changes during the gel densification gel into the final material. Considering the thermodynamics standpoint,

the decreasing free energy of the gel, due to the driving force resulted by high energy of the structure, is an irreversible process.

Denser materials allow for higher corrosion protection. However, high temperatures cannot be applied for curing operations due to the combustion of the organics as well as the adverse effect on the metallic substrates[93]. A process known as "densification" turns the less stable state into a more stable one, causing exothermic heat fluxes. This process is affected by gel microstructure and process parameters[95]. Under basic conditions or in the presence of higher water content, strongly branched cluster structures are formed that behave as discrete species prior to gelation. In the second case, gelation is carried out with the linking of the branched clusters in the colloidal form[96]. Physical ageing can be applied with DSC measurement which means gradual increment of heat. The heating rate requires careful arrangement depending on the nature of the polymer because long-term storage below Tg causes gradual molecular relaxation, in turn causing amorphic and abnormally dense polymer chains to form. Internal stress, embrittlement and dimensional changes occur due to the type of densification[97]. Therefore, no dwell temperature was applied around glass transition temperature.

The first region, endothermic peaks between 95 and 105 ºC of all samples showed the desorption of water-alcohol media in the matrix of the polymer. The peak was not evaluated as a water-alcohol media, where the coatings were dissolved. This is because the usage of a close hermetic pan prevented the peaks to form due to the volatilization of the media. The first small endothermic peaks developed as aging peaks due to water-alcohol desorption in the polymeric matrix and Tg for all samples. Next, structural relaxation started with the second endothermic peaks at the trailing edge of the Tg[98-99]. Ramis et. al.[100] achieved similar results in their curing attempt using DSC measurements. The melting temperature decreased with increasing amine content, which may be due to higher crosslinking in the polymeric matrix. The relaxation temperature of SP30 sample showed two peaks, which could be explained as non-bound POSS molecules to sol-gel network[101]. The exothermic peak at 120 ºC

was detected as polymerization temperature for all samples. In the light of this information, the temperatures for glass transition, network relaxation, and polymerization were confirmed by DSC measurements and the results were found as similar with the data given in literature.

4.4 Polymerization of Hybrid Coatings

In the sol-gel process, the concentration of GPTMS has a catalyst effect on the size and uniformity of resultant silica particles. The type of the catalyst is one of the important factors of silica growth. The acidic and basic catalysts drive the mechanisms which are cluster-cluster growth and cluster-monomer growth, respectively[102].

After the curing operation, the samples were named as SP000, SP101, SP201, and SP301. Cured sample measurements were completed using ATR-FTIR. As seen in Section 4.1, the aging of SP00 was discussed, and the reactions were evaluated based on the characteristic peaks. After curing, the peaks were expected to show disappearing or shifting behavior. All reactions were compared in the ranges of 3800-2600 cm^{-1} and 1800-600 cm^{-1}. No quantitative comparison was conducted. The region at 3800-2600 cm^{-1} was normalized by the peak at 2870 cm^{1}, which is a CH_2 antisymmetric stretching peak post-curing to achieve accurate sample comparisons in all cases. The detected 3742 cm^{-1} peak of the silanol group in GPTMS is expected to disappear after curing, assigned the formation of an Si-O-Si network. The characteristic epoxy ring signal in 3050-2990 cm^{-1} could not be evaluated during the aging time due to the presence of higher water-alcohol content. Such signals are commonly evaluated to detect the completion of the polymerization[80]. The identified peaks are shown in Figure 4.5. Their assignments are presented in Table 4.5.

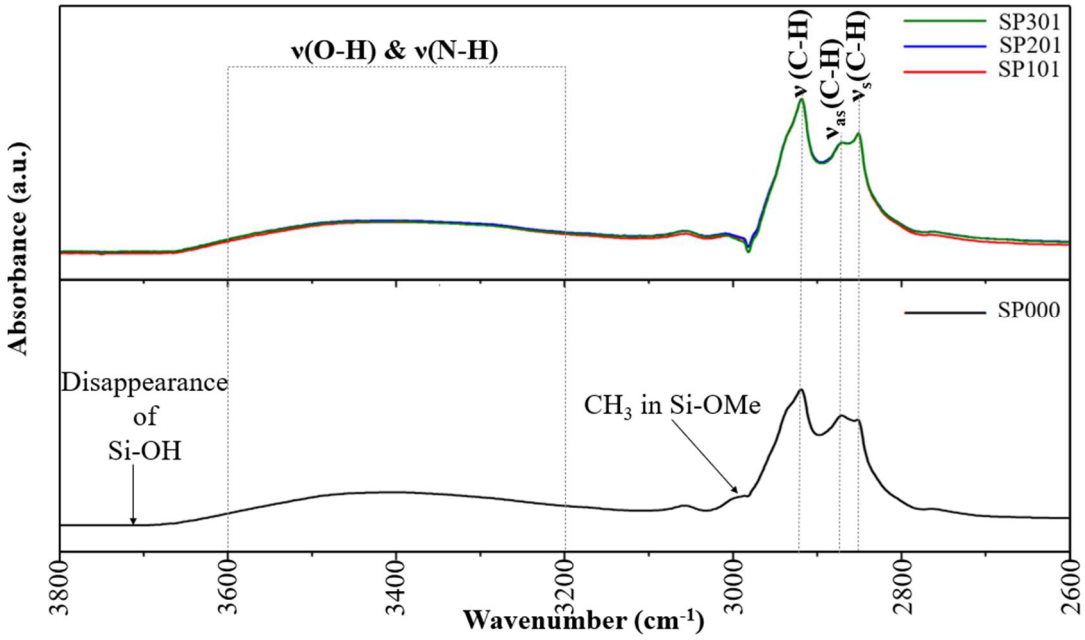

Figure 4.5. ATR-FTIR absorption spectra of all cured samples in the range of 3800-2600 cm^{-1}.

Table 4.5. Detected wavenumber and vibrational modes in the range of 3800-2600 cm^{-1} for all cured samples.

Wavenumber (cm^{-1})	**Vibrational Mode**	**References**
3600-3200	ν (O-H) and ν (N-H)	105
2929	ν (C-H) in $(C_2H_5O)_4Si$	104
2870	ν_{as}(C-H) of CH_2 in -CH_2O-	103
2840[103]	ν_s(C-H) of CH_2 in -CH_2O-	103

Stretching vibration; ν, symmetric; s, asymmetric; as.

The specified peak at 3742 cm^{-1} disappeared after heat treatment of SP000 sample. During the aging time, the peak had already disappeared in the amine content coatings starting from the 1st day. This absence may imply SP000 polymerization detectable be means of the characteristic Si-OH and Si-O-Si peaks in the fingerprint region. The stretching of hydroxyl and amine appears as overlapped species in the

range 3600-3400 cm^{-1} [105], making the assessment of polymerization virtually inaccurate. Even the characteristic amine peaks were not clearly observed in the overlapped region. After the analysis, the results showed the peak at 3464 and 3365 cm^{-1} due to N-H stretching. This shows the presence of the 1652 cm^{-1} below the 1800 cm^{-1} region[106]. As seen in Section 4.1, the aging of SP00, SP10, SP20, and SP30 in that region was addressed. The specified peaks were shown to shift to the right as the data presented in Table 4.5. The CH_3 stretching in Si-OMe group at 2987 cm^{-1} was detected in SP000 sample, which is attributed to incomplete polymerization. The peak was not observed in the amine-containing samples. However, full polymerization can be detected in the fingerprint region because the characteristic peaks are visible. The range of 1800-600 cm^{-1} was normalized by the peak at 1275 cm^{-1} for all samples. But no quantitative comparison was conducted. The characteristic peak signals of the epoxy group are shown in Figure 4.6. Their assignments are presented in Table 4.6.

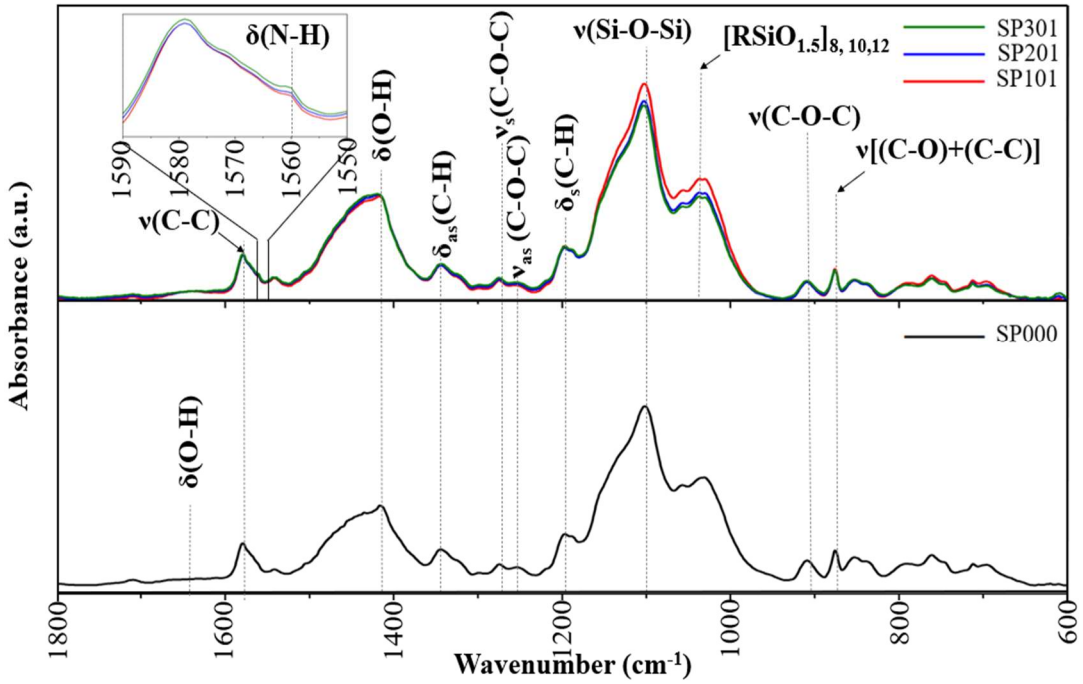

Figure 4.6. ATR-FTIR absorption spectra of all cured samples in the range of 1800-600 cm^{-1}. Inset spectral range: 1590-1550 cm^{-1}.

Table 4.6. Detected wavenumber and vibrational modes in the range of 3800-2600 cm^{-1} for all cured samples.

Wavenumber (cm^{-1})	**Vibrational Mode**	**References**
1650	δ(O-H)	107
1579	ν(C-C) due to crosslinking	108
1562	δ(N-H) due to epoxy ring - amine reaction	106
1417	δ_{as}(C-H) in $-CH_2-[-CH_2-(CO-)]$	109
1340	δ(O-H) in [-CH-O-]	104
1275	ν_{as} (C-O-C) due to crosslinking	108
1255	ν_s (C-O-C) due to crosslinking	108
1198	δ_{as}(C-H) in $-CH_2-[-CH_2-(CO-)]$	109
1100	ν(Si-O-Si)	109
1058	$[RSiO_{1.5}]_{8,\ 10,12}$	109
1030	ν (C-O)	109
910	ν(C-O-C) in due to epoxy ring functionalization	82
878	ν(C-O) + ν (C-C)	104

The O-H bending vibration at 1650 cm^{-1} was assigned as O-H groups in an unmodified hybrid film, as shown in Figure 4.6 for SP000 sample. The peaks were expected to fully disappear after heat treatment. The presence of the peak at 1650 cm^{-1} showed that unmodified O-H groups disappeared. This leads to decreasing water contact angle afterward and increasing surface wettability because unmodified hydroxyl groups cause the formation of hydrogen bonding with water molecules[107]. A small peak was also detected in 1700-1600 cm^{-1} for the amine content spectra, though a similar conclusion may not be deduced because the peak was also evaluated as an amide group in the hydrophobic side of the POSS. A characteristic N-H

bending peak was detected at 1562 cm^{-1} in the amine content spectra, showing the presence of a reaction between the opened epoxy ring and the amine side of the POSS. The peak at 1579 is assigned as a C-C stretching vibration[109], implying polymerization in the matrix. Other characteristic peaks of polymerization were determined at 1275 and 1255 cm^{-1} as antisymmetric and symmetric stretching of C-O-C, respectively[103]. The characteristic peak of the cage-structured POSS at 1058 cm^{-1} was detected as an overlapped stretching of C-C and C-O bonds, implying the presence of a C-C bond in the hydroxyl and a C-O bond in the cyclic species [109].

The specified peak of polymerization at 950 cm^{-1} shifted and remained at 910 cm^{-1}, which is either an epoxy or a silanol groups[15]. This further implies partial polymerization in all samples as well as closed epoxy rings remaining. This result is highly attributed to the curing temperature because disappearance is expected with increasing temperature[15]. The increasing temperature affected the polymeric coating inversely and causing boehmite structure formation ($AlOOH{\cdot}(OH)_x$), in turn preventing Al-O-Al bonds to form in octahedrally coordinated aluminum up to 120 ^oC[110]. A boehmite structure ($AlOOH{\cdot}(OH)_x$) leads to the hydrophilic surface property[110].

4.5 Thermal Property of Hybrid Coating

Commonly, the working conditions of aircraft structures change between -50 and 130 ^oC. For this reason, synthesized coatings were evaluated using DSC measurements after curing. No quantitative comparison was made, and the analysis was completed using a TA instrument program. The curves taken from DSC measurements are shown in Figure 4.7.

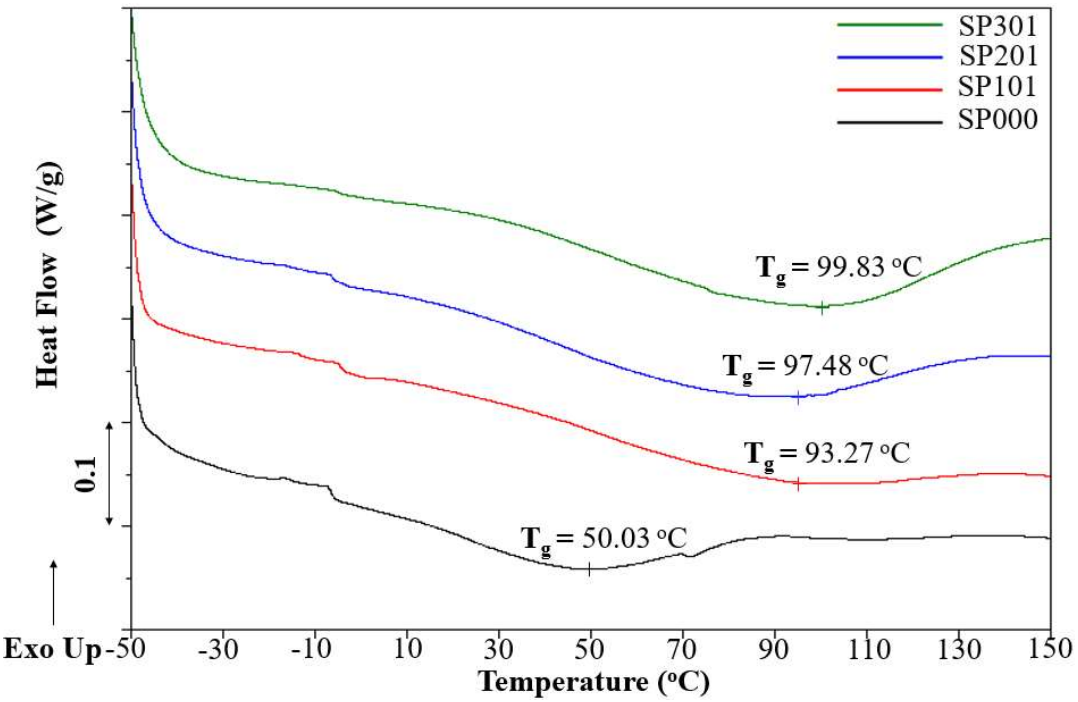

Figure 4.7. DSC curves of cured samples.

Thermally induced shape memory effects can show two types behavior in the polymeric structure: Cross-linked network and connecting onto the cross-linking sites of the switch segments[111]. Wang et. Al.[112] have been reported the relationship between glass transition temperature and shape memory effect. They proved increasing glass transition temperature due to shape memory of the material via thermally induced.

In this study, the active hydrogen side of the amino-functionalized POSS is cross-linked with an opened epoxy ring. No open cage POSS could be observed with FTIR measurement, and the lowest glass transition temperature of the coatings was determined in SP000 sample. Furthermore, no degradation peak was found, which may be considered unfavorable under given working conditions for synthesized coatings. Increasing the amine content provided for enhancing glass transition temperature due to the shape memory property of amino-functionalized POSS. Under the determined working conditions, the synthesized coatings did not show thermally stable behavior, despite thermally induced. When the thermally unstable

coatings interact with aluminum surfaces, they cause micro-cracks and afterward, become susceptible to corrosion. TMA measurements were carried out to examine such interactions. The values calculated are shown in Figure 4.8. The TMA curves of all samples are provided in Appendix A. The coefficient of thermal expansion (CTE) values was calculated automatically from the slope of the graph during measurements and presented in Table 4.7.

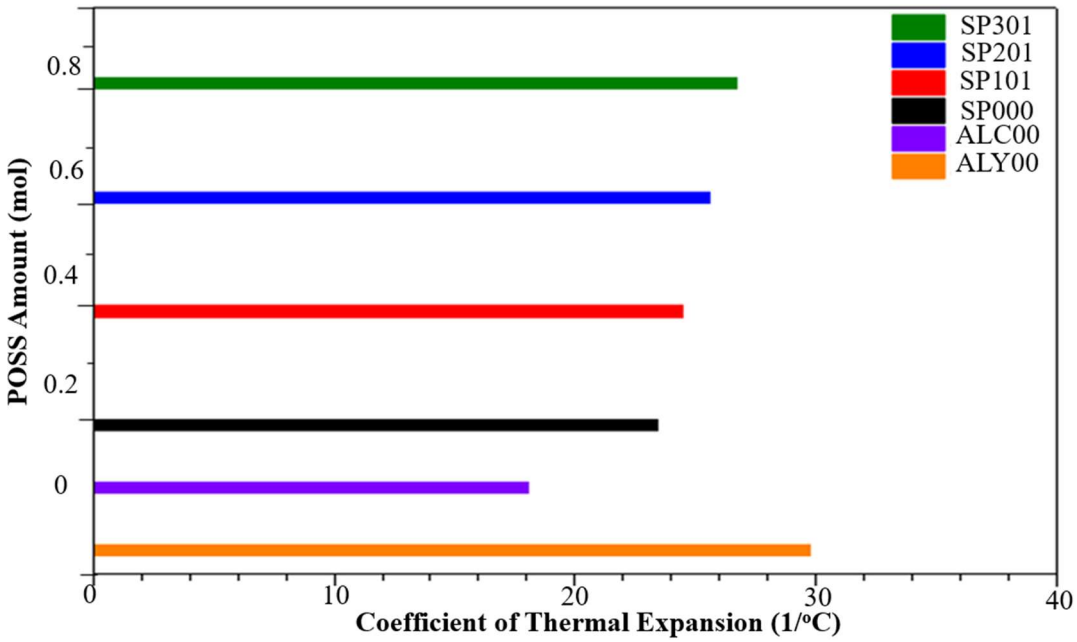

Figure 4.8. CTE values comparison according to the POSS amount of all samples.

Table 4.7. CTE values of all samples.

Samples	ALY00	ALC00	SP000	SP101	SP201	SP301
CTE (1/°C)	29.748	18.033	23.409	24.491	25.582	26.741

According to the AMS QQ-A 250/4 material specification, the thermal expansion of the aluminum 2024 T3 material is 23.1 1/°C [20]. But this value is applicable at temperature range between 20 and 100 °C. In order to evaluate the results under the same parameters, the CTE of a pre-penetrant etched applied sample was also measured. A CCC applied sample was detected as having the least expansion coefficient. When the coating works in between -50 and 130 °C conditions, it may

fail. Increasing the amine content allows for better thermal compatibility of the coating, although it could be different concerning the material characteristics of aluminum. This may be due to the organic side of the hybrid material because it does not allow further moving of the polymeric matrix. On the other hand, this property improves the mechanical property[54]. The experiment was carried under a constant heating rate, so higher amine content coating cannot be accounted for resistance against thermal shock. The result can be consolidated through dynamic mechanical analysis, which is not within the scope of the present work. The TMA measurements of all synthesized coated surfaces showed that the coatings worked compatibly with aluminum material in the temperature range from -50 ºC to 130 ºC working conditions at a constant heating rate of 10 ºC/min.

4.6 Surface Properties of Coating and Hydrophobicity

The coated surface thicknesses were determined by subtracting the sample thickness from the total thickness (sample thickness + coating thickness) after curing. Before doing so, the aluminum sample thickness and pre-penetrant etched aluminum sample surface were measured. The thickness of the Al 2024 T3 material was 1.020 mm as a standard material stock. After the etching process, the thickness decreased nearly 1 μm. Therefore, an immersion period of four minutes provided the average coating thickness of approximately 1 μm. The thicknesses were similar to the chemical conversion coating thickness of aluminum materials[113]. The roughness value of coating increased with increasing amount of amino-functionalized POSS. The data for both measurements are averaged. The roughness values of the samples are shown in Figure 4.9 and presented in Table 4.8.

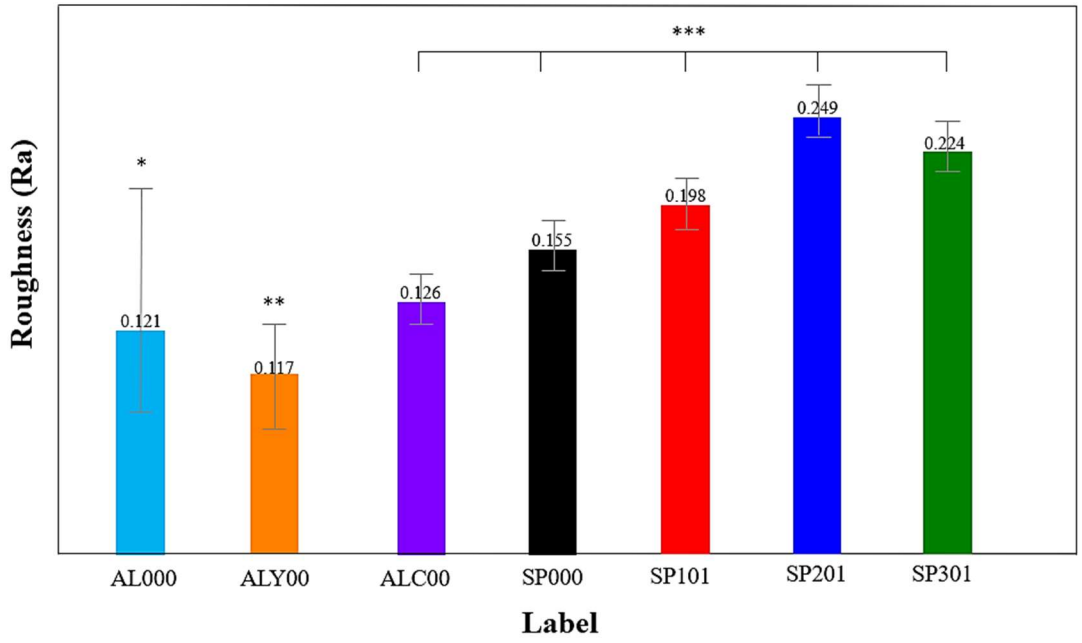

Figure 4.9. Roughness values of all coated samples. Standard Deviation: * = ± 0.08 Ra ; ** = ± 0.03 Ra ; *** = ± 0.02 Ra.

Table 4.8. Thickness and roughness of the samples.

Sample	**Thickness (mm)**	**Roughness (Ra)**
AL000	1.020± 0.00	0.121 ± 0.08
ALY00	1.019 ± 0.01	0.117 ± 0.03
ALC00	1.020 ± 0.01	0.126 ± 0.02
SP000	1.020 ± 0.01	0.155 ± 0.02
SP101	1.020 ± 0.01	0.198 ± 0.02
SP201	1.020 ± 0.01	0.249 ± 0.02
SP301	1.020 ± 0.01	0.224 ± 0.02

The thickness is related not only to the immersion time but also to the viscosity of the coating solution. One of the reasons for using the 95% ethanol solution was to

reduce the viscosity of coating solution and to obtain controlled surface roughness and homogeneity[114].

Considering the adhesion between the sol-gel films and the aluminum alloy surface, adhesion between coating and roughened surface occurs due to strong covalent bonds and mechanical interlocking. Additionally, the roughness of the coating surface is an important factor to improve adhesion between the surface and the primer topcoat application[115].

The roughness values of the coated surface are altered dramatically using a silica-based sol-gel coating application and the addition of amino-functionalized POSS in the sol-gel. Rahimi et al.[116] showed that increasing surface roughness was attributed to the inorganic content of the coating. Improved flexibility and reduced defects are possible with organic components, leading to low surface roughness. They also reported that increasing hardness causes reduced surface roughness in the presence of inorganic and organic components together.

A thick and inhomogeneous coating is not preferable due to the tendency for crack formation. Increasing film thickness and heterogenicity causes changes in crack spacing. The mechanism of the behavior attributes partial delamination failure and causes crack propagation. This phenomenon is observed when cracks formed in the sol-gel silicate film on the surface[49].

Surface morphology is one of the most important factors in coating. Hybrid polymeric coatings on the surface cause cracks or pores when the heating rate is not optimized. When this rate accelerates to release gases during polymerization, this causes corrosion on the aluminum surface, such as pitting[117-118]. However, non-homogenous and porous surfaces also increase roughness and lead to reduced contact angle. The SEM images of reference samples, ALY00 and ALCOO and their contact angle measurements are provided in Figure 4.10.

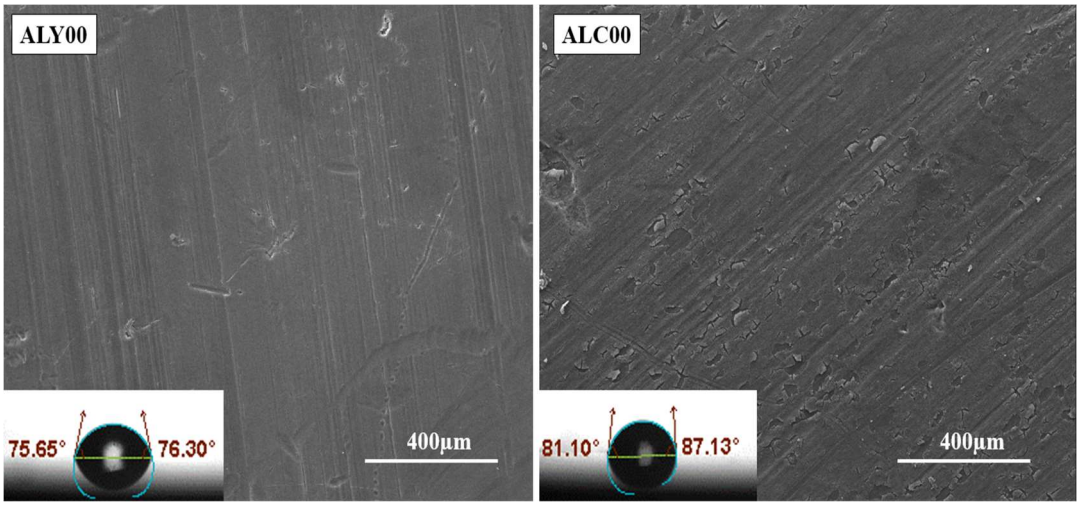

Figure 4.10. SEM images and contact angle measurement of reference samples.

ALY00 sample showed scratch signs on the surface, although pre-penetrant etch was applied not only to prevent scratch but also to obtain a uniform surface. When comparing the standard deviation of AL000 and ALY00, the declining deviation of the latter resulted in a more uniform surface after the etching process. ALC00 sample has a surface coated with chemical conversion, a technique commonly used in the aerospace industry. In Figure 4.10, the sample shows non-uniform and locally flaked surfaces. The two surfaces showed hydrophilic surface properties, although the CCC applied surface had an increased contact angle.

After the sol-gel based coating application, the roughness values of the coated surfaces improved. The increment provided hydrophobic surface property for SP201 and SP301, while it caused hydrophilicity for SP000 and SP101. The SEM images of the sol-gel-based coating with their contact angle measurements shown in Figure 4.11.

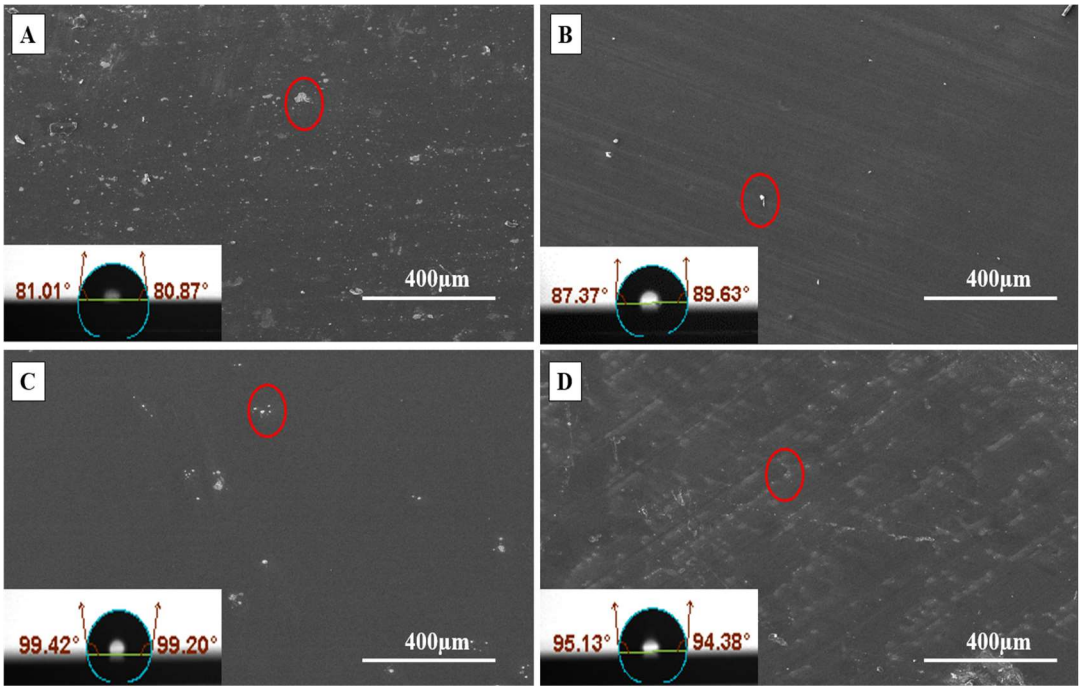

Figure 4.11. SEM images with contact angle measurements of coated samples (A: SP000, B: SP101, C: SP201, D: SP301).

According to the images, no cracks occurred during the curing process, a result also supported by contact angle measurements. Red circles show silica particles. In SP301 which has a higher degree of polymerization, the particles showed closer and better disperse surface property.

The contact angle of a surface is related to the chemical properties of coating and surface morphology. Contrary to popular myth, Wu et al.[119] reported that increasing surface roughness increases the water contact angle and cause hydrophobicity. The presence of a silica filler causes increased solid content in the coating, leading to a rougher surface. After the ring opening of GPTMS with a basic precursor, a semi-crystalline structure causes a rise in the solid content of sol-gel during the coating condensation. This can be observed as a non-bonded opened epoxy ring with amino-functionalized POSS. Roughness and contact angle values were related except samples SP000 and SP101.

According to Wenzel's theory, there is an inversely related between contact angle and roughness when the former is measured below 90º. The contact angle below 90º for SP000 and SP101 was found to be hydrophilic, as shown in Figure 4.10-A and B. Hydrophilicity is directly related to the opened epoxy ring on the coated surfaces. Cross-linking between two networks can be accomplished during the curing operation, and it requires an epoxy ring and silanol reaction or the hydroxyl of the opened epoxy rings and silanol by condensation[120]. For the SP101 sample, the addition of POSS did not prevent hydrophilicity due to epoxy rings that were left open. The addition of POSS made the coating surface type close to the boundary of non-wetting, causing the coating to become hydrophobic.

Since the hydrophobic side of the amino-functionalized POSS affected both roughness and the contact angle in a positive manner[121], it increments of POSS content was also expected to affect the roughness and hydrophobicity. SP201 in Figure 4.11-C showed the best hydrophobic characteristic among the other samples, which was due to cross-linking and polymerization of the coating and aluminum surface[122]. The hydrophobic side of the amino-functionalized POSS may cause solid/liquid content in the coating assumed as a composite configuration in the interface. According to Bico's theory, air is trapped, and the liquid is no longer fully diffused into the protrusions of surface, even when the contact angle is measured below 90º [123]. The decreasing contact angle in SP301 could be caused due to the reaction of all opened rings with the amine group of amino-functionalized POSS, while the remained-opened epoxy rings caused the hydrophilicity in SP000 and SP101 samples. This could be due to a drop in cross-linking between the coating and the aluminum surface. However, SP201 and SP301 have a hydrophobic character. As a result, hydrophobicity can be effectively measured with corrosion experiments since it is considered as a function of corrosion resistance in this research.

4.7 Adhesion Performance of Coating

The adhesion performance of the cured coatings was evaluated with an adhesion test. The test is generally used to evaluate primers and topcoats' adhesion performance with the metallic surface in the aerospace industry. The coatings synthesized have a polymeric nature. Hence, the test can give accurate information about the adhesion quality of the coatings. Given the SEM images in Section 4.6, no cracks were observed, implying no susceptibility to corrosion. The adhesion test images for SP000 and SP301 samples are shown in Figure 4.12. The images for the other samples are presented in Appendix B. SP000 sample showed the least polymerization with respect to the FTIR measurements, whereas SP301 showed better performance among the amine content coatings.

The tests were completed two weeks after coating. According to the NEN-EN-ISO 2409 standard-Class 0, "the edges of the cuts are completely smooth; none of the squares of the lattice is detached".

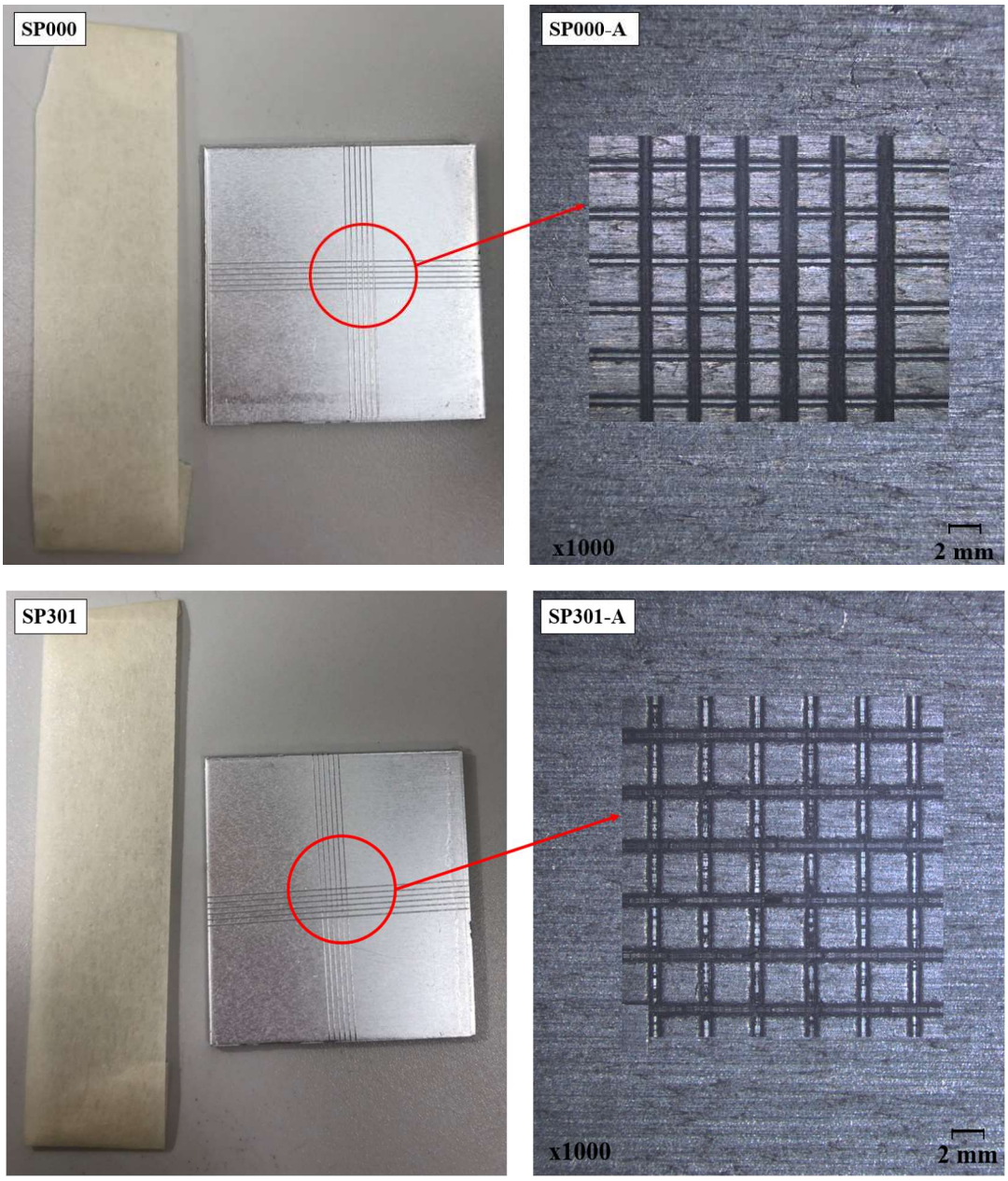

Figure 4.12. Adhesion test images of SP000 and SP301 samples.

No empty lattice was detected in any case, but the appearance of the coating may have made it difficult to view the lattices; however, no left-over coating on the tape or color changes were detected, either, showing that all the synthesized coatings adhered to the aluminum surface properly.

4.8 Corrosion Performance of Coating

The corrosion performance of the cured coatings was evaluated with electrochemical impedance spectroscopy (EIS) tests. The corrosion behavior of metal is thoroughly analyzed with the electrochemical method, and the corresponding interactions between the metal surface and electrolyte solution are detected using EIS. According to the related principles, reduction and oxidation processes on the metal surface occurred simultaneously in a corrosive environment, and the oxidized (corroded) materials are the solvent and the specimen. The specimen surface should both serve as anodic and cathodic, to allow respective currents to pass along the specimen surface together. Generally, corrosion occurs due to the anodic currents. When the two currents are equal in magnitude on the surface, there is potential for corrosion potential, denoted as E_{corr}. The E_{corr}, rates of oxidation and reduction in a specimen are equal, but polarity is more positive than the corrosion potential (E_{corr}) when the anodic current is predominant. Increasing the magnitude of polarity causes the cathodic current to be neglected. The potentiodynamic polarization plot is obtained from the log current function vs the potential chart. The E_{corr} is negative, which causes enhancement of the cathodic current. The anodic current with a positive potential is a reverse case in this regard[124].

In this research, all the data were calculated, and plots were drawn using computer programs. The background to computations and the equations are seen in Section 3.4.8. The coated sample plots were evaluated in Figure 4.13 with a Nyquist plot and in Figure 4.14 with a Tafel plot. For all coated samples, fresh measurements were completed, and the experiment were carried out for 48 hours. The plots and Tafel fits of each sample are shown in Appendices C.1, C.2, C.3, and C.4.

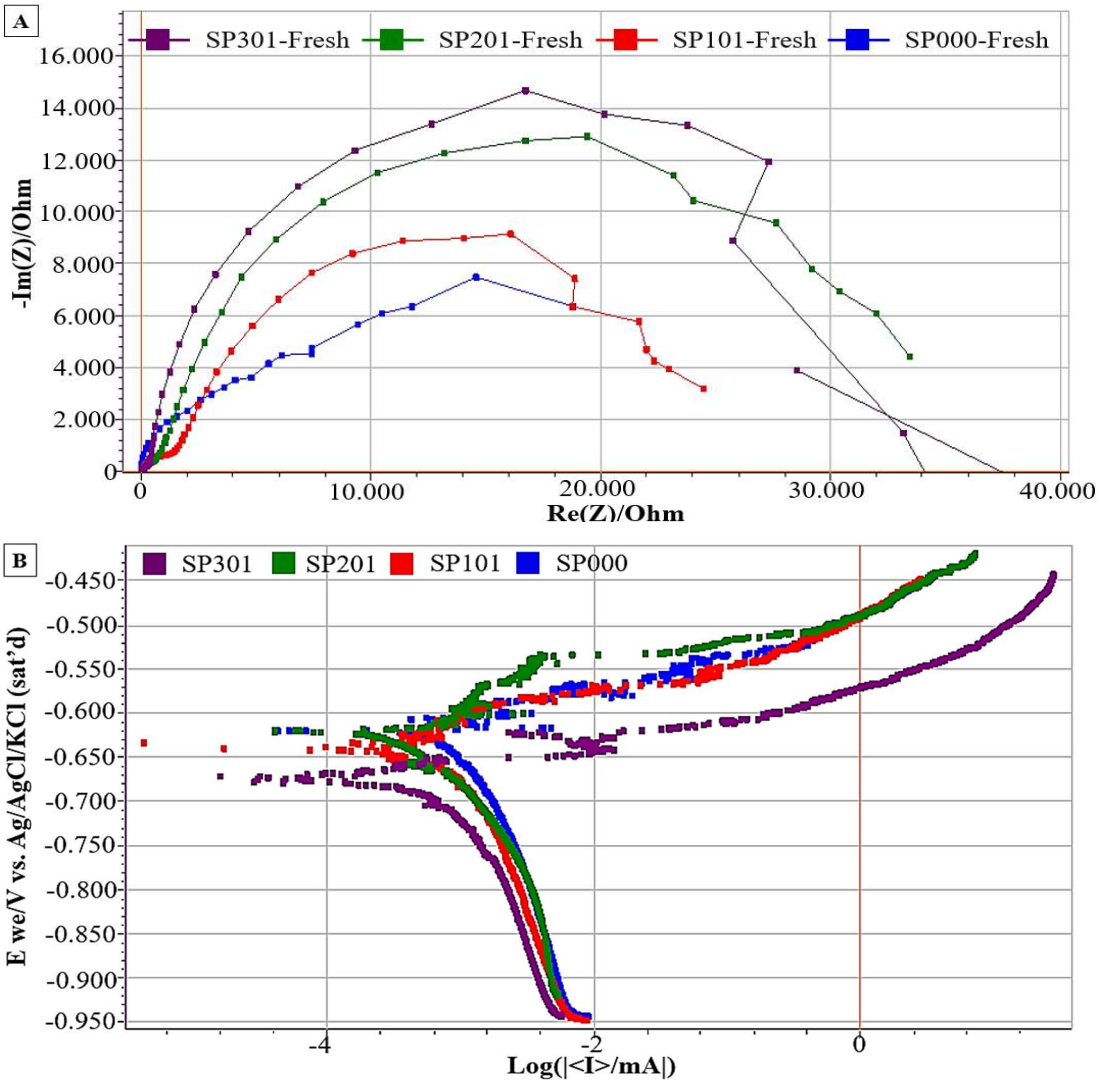

Figure 4.13. A:Nyquist plot of all samples; B:Tafel plot of all samples.

Polarization resistance or linear polarization (Rp) is used to measure absolute corrosion rates. This electrochemical technique measures absolute corrosion rates rapidly. Precise correlations need to be made between polarization resistance and the determination of conventional weight loss. The corrosion current i_{CORR} and corrosion are highly related to each other as well. Hence, calculated with Eq.1 and Eq.2, respectively[125].

According to mixed potential theory, two or more oxidation and reduction reactions take place during electrochemical reactions without any accumulation of electrical

charge and any externally applied potential. The rate of oxidation and reduction in the corroding system are evaluated equal in magnitude, whereas the current is calculated as zero using Eq.3. No external application of potential systems is also knowns as an open circuit potential (OCP) and expressed as E_{CORR}. The reaction rate is under control by a slow step of chemical reaction that needs activation energy as an external voltage source applied on the metal. Here, mixed potential theory is evaluated using Eq. 5 and Eq. 6 theoretically based on Eq. 4 and at the equilibrium of reaction[75]. Before the evaluation of the sample corrosion resistance, ALY00 and ALC00 were measured for the corrosion rate with reference as presented in Table 4.9.

Table 4.9. Reference sample for corrosion evaluation of the coated samples.

Sample Name	**E_{CORR} (mV)**	**I_{CORR} (mA)**	**β_a (mV)**	**β_c (mV)**	**Corrosion Rate (mmpy)**
ALY00	-553.715	7.556	15.6	1082	32.90×10^{-3}
ALC00	-1067	1.350	455.6	150.0	5.88×10^{-3}

The calculated different corrosion parameters for all coated samples are tabulated in Table 4.10. Accordingly, E_{CORR} of the reference sample was calculated as negative, which shows more anodic properties than the coated samples.

Table 4.10. Corrosion evaluation of all samples after 48 h.

Sample Name	**E_{CORR} (mV)**	**I_{CORR} (mA)**	**β_a (mV)**	**β_c (mV)**	**Corrosion Rate (mmpy)**
SP000	-619.727	1.133	42.2	376.2	4.93×10^{-3}
SP101	-636.593	1.025	44.5	379.9	4.62×10^{-3}
SP201	-622.599	0.733	147.1	281.2	3.19×10^{-3}
SP301	-682.625	1.087	37.1	384.9	4.73×10^{-3}

According to the reference measurements for bare aluminum sample E_{CORR} was measured as -0.55 V. Considering all coated samples, the E_{CORR} rate was more negative, meaning more cathodic than the bare aluminum sample and more anodic than the CCC coated sample. This could mean that the organic inhibitors lead to preventing cathodic reactions with water or O_2, which stay immobilized on copper. When Cu(I) complexes are formed with organic inhibitors due to the presence of copper content on the surface of the aluminum material, these complexes prevent any reaction with corrosive environments[126]. CCC coating has more cathodic than the coated samples, which may be due to have electrical conductivity.

Metroke et al.[127] have shown the relation between the corrosion potential, Ecorr, and the chain length of amine in GPTMS/TEOS systems. The curing process for these systems is carried out with different amines such as diethylenetriamine, triethylenetetraamine, tetraethylenepentamine, etc. and the reduction of E_{CORR}, is shown to be attributed to longer amine chains by means of increasing amine functionalities. Therefore, enhancing the possibility of the formation of amino complexes on the copper rich contained AA 2024 surface leads to a reduction in the corrosion potential.

Concerning the corrosion potential of SP000 sample shows the lowest corrosion resistance among other samples (SP101, SP201, and SP301) because the opened epoxy ring on the surface increases the hydrophilicity, exposing the surface to corroding agents[66]. The SP000, SP101, SP201, and SP301 samples showed better corrosion performance compared with the bare aluminum reference sample. The calculated corrosion rates of all coated samples were found to be less than the bare aluminum since increasing the organic content of the coating revealed dielectric properties and preventing electron transfer, except in SP201[126]. This sample was found to have the highest hydrophobic property and, as such, is expected to have higher corrosion performance. Though this effect could not be observed because trapped air in SP201 sample escaped by means of corrosive ions and water diffusion. Hence, having the lowest corrosion potential among all the amino-functionalized, POSS-contained coatings.

CHAPTER 5

CONCLUSIONS AND FUTURE WORKS

5.1 Conclusions

A sol-gel reaction between the 3-Glycidoxypropyltrimethoxysilane (GPTMS) and 0.2, 0.4, and 0.6 mol amino functionalized and 50% amphiphilic polyhedral oligomeric silsesquioxane (POSS) is performed under extreme basic conditions. Epoxy ring of GPTMS is opened via basic sol-gel process. T10 cage structure amino-functionalized POSS are used as a curing agent. An optimum aging time for the completion of the sol-gel reactions as determined by FTIR measurements is 6 days. A higher degree of polymerization is obtained for GPTMS including amine POSS as compared to GPTMS basic sol-gel. The amino functionalized POSS included GPTMS could be successfully applied on an aluminum alloy, Aluminum 2024-T3, by immersion technique. Scanning electron microscope examinations reveal that crack free coatings could be applied on Aluminum 2024-T3 sample. No degradation of coating is noticed at the service temperature of aircraft structure for all the POSS included GPTMS prepared. Higher amine POSS containing coatings has more or less the same thermal expansion coefficient with Aluminum 2024-T3. Contact angle measurements reveal that contact angle is more than 90^{o} for the coating applied on Aluminum 2024-T3 sample for the coatings produced by immersing into solutions including 0.4 mol and 0.6 mol amino functionalized POSS for 4 min subsequently cured at 120 ^{o}C for 60 min. That is, SP201 and SP301. The Aluminum 2024-T3 samples coated by immersing into solutions containing no or lesser amount of amino functionalized POSS, SP000 and SP101, exhibit contact angles less than 90^{o}, implying partial polymerization of the network.

Surface roughness increases as the amount of amino functionalized POSS included increases. SP201 offers roughness, and contact angle among the all the samples

prepared. Enhancement of roughness also paved the way for adhesion performance. Primer and topcoat application ensured the resistance against the chemical corrosion more effectively. Enhanced adhesion performance provides more positively to the surface corrosion resistance when presence of primer and topcoat applications. Corrosion performance of the GPTMS prepared has been elucidated using electrochemical impedance spectroscopy. Surprisingly, although SP201 has better hydrophobic character, its corrosion performance is worse than SP301 as a result of escape of trapped air in the network. SP301 show better corrosion performance among all the coated samples. In terms of the surface properties and corrosion behavior a GPTMS:Amino functionalized POSS molar ratio of 1:0.6 has been proven the best coating ratio. Increasing amount of amino functionalized POSS facilitates the possibility of the network formation and improves corrosion resistance of bare aluminum surface. In spite of good peculiarities, amine added coatings have limited usage for aircraft structure since thermally treated coatings may decrease fatigue resistance of the Aluminum 2024-T3.

5.2 Future Works

Thermal expansion is an important factor in the service conditions of aircraft structures. Nevertheless, thermal shock resistance cannot be detected by itself with TMA measurements. A dynamic mechanical analysis will be completed for all coated samples and thermal shock resistance and mechanical properties should be evaluated as well. According to the MIL-DTL-5541 spec of chemical conversion coating, the salt spray test can be a key determiner of corrosion performance of coatings. Beside the EIS measurements, corrosion performance should also be evaluated by using salt spray test in future to determine the working life better for such coatings.

REFERENCES

(1) Zhang, J.; Zhao, X.; Zuo, Y.; Xiong, J. The Bonding Strength and Corrosion Resistance of Aluminum Alloy by Anodizing Treatment in a Phosphoric Acid Modified Boric Acid / Sulfuric Acid Bath. *Surf. Coatings Technol.* **2008**, *202* (14), 3149–3156.

(2) Augustin, C.; Andrieu, E.; Blanc, C.; Mankowski, G.; Delfosse, J. Intergranular Corrosion of 2024 Alloy in Chloride Solutions. *J. Electrochem. Soc.* **2007**, *154* (11), C637.

(3) Park, S. Y.; Choi, W. J.; Choi, H. S.; Kwon, H.; Kim, S. H. Recent Trends in Surface Treatment Technologies for Airframe Adhesive Bonding Processing: A Review (1995-2008). *J. Adhes.* **2010**, *86* (2), 192–221.

(4) Skeldon, P.; Thompson, G. E.; Habazaki, H. A Tracer Investigation of Chromic Acid Anodizing of Aluminium. *Surf. Interface Anal. An Int. J. devoted to Dev. Appl. Tech. Anal. surfaces, interfaces thin Film.* **2007**, *39* (11), 860–864.

(5) Harscoet, E.; Froelich, D. Use of LCA to Evaluate the Environmental Benefits of Substituting Chromic Acid Anodizing (CAA). *J. Clean. Prod.* **2008**, *16* (12), 1294–1305.

(6) Foley, R. T. Localized Corrosion of Aluminum Alloys - A Review. *Corrosion* **1986**, *42* (5), 277–288.

(7) Makhlouf, A. S. H. Current and Advanced Coating Technologies for Industrial Applications. *Nanocoatings Ultra-Thin Film. Technol. Appl.* **2011**, 3–23.

(8) Wang, D.; Bierwagen, G. P. Sol–Gel Coatings on Metals for Corrosion Protection. *Prog. Org. Coatings* **2009**, *64* (4), 327–338.

(9) Figueira, R. B.; Silva, C. J. R.; Pereira, E. V. Organic – Inorganic Hybrid Sol – Gel Coatings for Metal Corrosion Protection : A Review of Recent Progress. **2015**, *12* (1), 1–35.

(10) Zheludkevich, M. L.; Serra, R.; Montemor, M. F.; Miranda Salvado, I. M.; Ferreira, M. G. S. Corrosion Protective Properties of Nanostructured Sol-Gel Hybrid Coatings to AA2024-T3. *Surf. Coatings Technol.* **2006**, *200* (9), 3084–3094.

(11) Hirano, S. Improvement of Corrosion Resistance of Metals by an Environmentally Friendly Silica Coating Method. *J. Sol-Gel Sci. Technol.* **2004**, *29* (3), 147–153.

(12) Innocenzi, P.; Figus, C.; Kidchob, T.; Valentini, M.; Alonso, B.; Takahashi, M. Sol-Gel Reactions of 3-Glycidoxypropyltrimethoxysilane in a Highly Basic Aqueous Solution. *J. Chem. Soc. Dalt. Trans.* **2009**, No. 42, 9146–

9152.

(13) Russo, L.; Gabrielli, L.; Valliant, E. M.; Nicotra, F.; Jiménez-barbero, J.; Cipolla, L.; Jones, J. R. Novel Silica/Bis (3-Aminopropyl) Polyethylene Glycol Inorganic/Organic Hybrids by Sol-Gel Chemistry. *Mater. Chem. Phys.* **2013**, *140* (1), 168–175.

(14) Taylor, P.; Wu, J.; Mather, P. T. POSS Polymers : Physical Properties and Biomaterials Applications POSS Polymers : Physical Properties and Biomaterials Applications. *Polym. Rev.* **2009**, *49* (1), 37–41.

(15) Jerman, I.; Šurca Vuk, A.; Koželj, M.; Švegl, F.; Orel, B. Influence of Amino Functionalised POSS Additive on the Corrosion Properties of (3-Glycidoxypropyl)Trimethoxysilane Coatings on AA 2024 Alloy. *Prog. Org. Coatings* **2011**, *72* (3), 334–342.

(16) Jawalkar, C. S., & Kant, S. A Review on Use of Aluminium Alloys in Aircraft Components. *i-Manager's J. Mater. Sci.* **2015**, *3* (3), 33.

(17) Husaini, M.; Usman, B.; Ibrahim, M. B. Evaluation of Corrosion Behaviour of Aluminum in Different Environment. *Bayero J. Pure Appl. Sci.* **2019**, *11* (1), 5.

(18) Landolt, D. *Corrosion and Surface Chemistry of Metals*, 1st ed.; 522 p., 2007.

(19) Pakes, A.; Thompson, G. E.; Skeldon, P.; Morgan, P. C. Development of Porous Anodic Films on 2014-T4 Aluminium Alloy in Tetraborate Electrolyte. **2014**, *45* (2003), 1275–1287.

(20) QQ-A-250/4 "T3" Sheet Data Sheet http://www.aerometalsalliance.com/resources/data-sheets/view/Aluminium-Alloy-QQ-A-2504-T3-Sheet_197 (accessed Oct 13, 2021).

(21) QQ-A-250/5 "T3" Sheet Data Sheet http://www.aerometalsalliance.com/resources/data-sheets/view/Aluminium-Alloy-QQ-A-2505-T3-Sheet_201 (accessed Oct 13, 2021).

(22) Gao, M.; Feng, C. R.; Wei, R. P. An Analytical Electron Microscopy Study of Constituent Particles in Commercial 7075-T6 and 2024-T3 Alloys. *Metall. Mater. Trans. A Phys. Metall. Mater. Sci.* **1998**, *29* (4), 1145–1151.

(23) Shao, M.; Fu, Y.; Hu, R.; Lin, C. A Study on Pitting Corrosion of Aluminum Alloy 2024-T3 by Scanning Microreference Electrode Technique. *Mater. Sci. Eng. A* **2003**, *344* (1–2), 323–327.

(24) Huang, I. W.; Hurley, B. L.; Yang, F.; Buchheit, R. G. Dependence on Temperature, PH, and Cl- in the Uniform Corrosion of Aluminum Alloys 2024-T3, 6061-T6, and 7075-T6. *Electrochim. Acta* **2016**, *199*, 242–253.

(25) Clark, W. J.; Ramsey, J. D.; McCreery, R. L.; Frankel, G. S. A Galvanic

Corrosion Approach to Investigating Chromate Effects on Aluminum Alloy 2024-T3. *J. Electrochem. Soc.* **2002**, *149* (5), B179.

(26) Su, P.; Devereux, O. F. Impedance Characterization of Crevice Corrosion of an Aluminum 2024 Structure. *Corrosion* **2003**, *59* (9), 780–789.

(27) Abbass, M. K.; Habeeb, H. M. Study of Erosion-Corrosion and Electrochemical Corrosion in Some Aluminum Alloys (Al 2024T3 and Al 7075T6). *Int. J. Energy Environ.* **2016**, *8* (6), 545–556.

(28) Cabrini, M.; Bocchi, S.; D'Urso, G.; Giardini, C.; Lorenzi, S.; Testa, C.; Pastore, T. Stress Corrosion Cracking of Friction Stir-Welded AA-2024 T3 Alloy. *Materials (Basel).* **2020**, *13* (11), 2610.

(29) Salvarezza, R. C.; de Mele, M. F. L.; Videla, H. A. Mechanisms of the Microbial Corrosion of Aluminum Alloys. *Corrosion* **1983**, *39* (1), 26–32.

(30) Twite, R. L.; Bierwagen, G. P. Review of Alternatives to Chromate for Corrosion Protection of Aluminum Aerospace Alloys. **1998**, *33*, 91–100.

(31) Abrahami, S. T.; de Kok, J. M. M.; Terryn, H.; Mol, J. M. C. Towards Cr(VI)-Free Anodization of Aluminum Alloys for Aerospace Adhesive Bonding Applications: A Review. *Front. Chem. Sci. Eng.* **2017**, *11* (3), 465–482.

(32) Brockmann, W.; Hennemann, O. D.; Kollek, H.; Matz, C. Adhesion in Bonded Aluminium Joints for Aircraft Construction. *Int. J. Adhes. Adhes.* **1986**, *6* (3), 115–143.

(33) Fullen, W. J.; Deheck, J. Aluminum Metal Surface Finishing Corrosion Causes and Troubleshooting. *Natl. Assoc. Surf. Finish. Annu. Conf. Trade Show, SUR/FIN 2014* **2014**, *79* (December), 320–348.

(34) G.E, T. Porous Anodic Alumina: Fabrication, Characterization and Applications. *Thin Solid Films* **1997**, *297*, 192–201.

(35) Keller, F.; Hunter, M. S.; Robinson, D. L. Structural Features of Oxide Coatings on Aluminum. *J. Electrochem. Soc.* **1953**, *100* (9), 411.

(36) Critchlow, G. W.; Yendall, K. A.; Bahrani, D.; Quinn, A.; Andrews, F. Strategies for the Replacement of Chromic Acid Anodising for the Structural Bonding of Aluminium Alloys. *Int. J. Adhes. Adhes.* **2006**, *26* (6), 419–453.

(37) Kendig, M. W.; Davenport, A. J.; Isaacs, H. S. The Mechanism of Corrosion Inhibition by Chromate Conversion Coatings from X-Ray Absorption near Edge Spectroscopy (XANES). *Corros. Sci.* **1993**, *34* (1), 41–49.

(38) Olsson-Jacques, C. L.; Wilson, A. R.; Rider, A. N.; Arnott, D. R. Effect of Contaminant on the Durability of Epoxy Adhesive Bonds with Alclad 2024 Aluminium Alloy Adherends. *Surf. Interface Anal.* **1996**, *24* (9), 569–577.

(39) Kinloch, A. J.; Little, M. S. G.; Watts, J. F. Role of the Interphase in the Environmental Failure of Adhesive Joints. *Acta Mater.* **2000**, *48* (18–19), 4543–4553.

(40) Abel, M. L.; Digby, R. P.; Fletcher, I. W.; Watts, J. F. Evidence of Specific Interaction between γ-Glycidoxypropyltrimethoxysilane and Oxidized Aluminum Using High-Mass Resolution ToF-SIMS. *Surf. Interface Anal. An Int. J. devoted to Dev. Appl. Tech. Anal. surfaces, interfaces thin Film.* **2000**, *29* (2), 115–125.

(41) Franquet, A.; Terryn, H.; Vereecken, J. Study of the Effect of Different Aluminium Surface Pretreatments on the Deposition of Thin Non-Functional Silane Coatings. *Surf. Interface Anal.* **2004**, *36* (8), 681–684.

(42) Kinloch, A. J.; Welch, L. S.; Bishop, H. E. The Locus of Environmental Crack Growth in Bonded Aluminium Alloy Joints. *J. Adhes.* **1984**, *16* (3), 165–177.

(43) Kock E, Muss V, Matz C, D. W. F. Process for Anodic Oxidation. Patent EP0607579A1·1994-07-27, 1994.

(44) Abrahami, S. T.; Hauffman, T.; De Kok, J. M. M.; Mol, J. M. C.; Terryn, H. XPS Analysis of the Surface Chemistry and Interfacial Bonding of Barrier-Type Cr(VI)-Free Anodic Oxides. *J. Phys. Chem. C* **2015**, *119* (34), 19967–19975.

(45) Abrahami, S. T.; de Kok, J. M. M.; Gudla, V. C.; Ambat, R.; Terryn, H.; Mol, J. M. C. Interface Strength and Degradation of Adhesively Bonded Porous Aluminum Oxides. *NPJ Mater. Degrad.* **2017**, *1* (1).

(46) García-Rubio, M.; Ocón, P.; Climent-Font, A.; Smith, R. W.; Curioni, M.; Thompson, G. E.; Skeldon, P.; Lavía, A.; García, I. Influence of Molybdate Species on the Tartaric Acid/Sulphuric Acid Anodic Films Grown on AA2024 T3 Aerospace Alloy. *Corros. Sci.* **2009**, *51* (9), 2034–2042.

(47) Curioni, M.; Skeldon, P.; Koroleva, E.; Thompson, G. E.; Ferguson, J. Role of Tartaric Acid on the Anodizing and Corrosion Behavior of AA 2024 T3 Aluminum Alloy. *J. Electrochem. Soc.* **2009**, *156* (4), C147.

(48) Hennemann, O. D.; Brockmann, W. Surface Morphology and Its Influence on Adhesion. *J. Adhes.* **1981**, *12* (4), 297–315.

(49) Brinker, C. J.; Hurd, A. J.; Schunk, P. R.; Frye, G. C.; Ashley, C. S. Review of Sol-Gel Thin Film Formation. *J. Non. Cryst. Solids* **1992**, *147–148* (C), 424–436.

(50) Brincker, C Jeffrey; Scherer, G. W. The Sol-Gel Process. *Chem. Rev.* **1990**, *90* (1), 33–72.

(51) Schmidt, H. Chemistry of Material Preparation by the Sol-Gel Process. *J.*

Non. Cryst. Solids **1988**, *100* (1–3), 51–64.

(52) Figueira, R. B.; Fontinha, I. R.; Silva, C. J. R.; Pereira, E. V; Figueira, R. B.; Fontinha, I. R.; Silva, C. J. R.; Pereira, E. V. Hybrid Sol-Gel Coatings: Smart and Green Materials for Corrosion Mitigation. *Coatings* **2016**, *6* (1), 12.

(53) Wen, J.; Wilkes, G. L. Organic/Inorganic Hybrid Network Materials by the Sol-Gel Approach. *Chem. Mater.* **1996**, *8* (8), 1667–1681.

(54) Chou, T. P.; Chandrasekaran, C.; Cao, G. Z. Sol-Gel-Derived Hybrid Coatings for Corrosion Protection. *J. Sol-Gel Sci. Technol.* **2003**, *26* (1–3), 321–327.

(55) Schmidt, H.; Scholze, H.; Kaiser, A. Principles of Hydrolysis and Condensation Reaction of Alkoxysilanes. *J. Non. Cryst. Solids* **1984**, *63* (1–2), 1–11.

(56) Wen, J.; Dhandapani, B.; Oyama, S. T.; Wilkes, G. L. Preparation of Highly Porous Silica Gel from Poly(Tetramethylene Oxide)/Silica Hybrids. *Chem. Mater.* **1997**, *9* (9), 1968–1971.

(57) Avnir, D.; Kaufman, V. R. Alcohol Is an Unnecessary Additive in the Silicon Alkoxide Sol-Gel Process. *J. Non. Cryst. Solids* **1987**, *92* (1), 180–182.

(58) Ying, J. Y.; Benziger, J. B.; Navrotsky, A. Structural Evolution of Alkoxide Silica Gels to Glass: Effect of Catalyst PH. *J. Am. Ceram. Soc.* **1993**, *76* (10), 2571–2582.

(59) Tiwari, I.; Mahanwar, P. A.; Tiwari, I.; Mahanwar, P. A. Polyacrylate / Silica Hybrid Materials : A Step Towards Multifunctional Properties. *J. Dispers. Sci. Technol.* **2019**, *40* (7), 925–257.

(60) Nicotra, F.; Cipolla, L.; Jones, J. R. RSC Advances Exploring GPTMS Reactivity against Simple Nucleophiles : Chemistry beyond Hybrid Materials. **2014**, 1841–1848.

(61) Templin, M.; Wiesner, U.; Spiess, H. W. Multinuclear Solid-State-NMR Studies of Hybrid Organic-Inorganic Materials. *Adv. Mater.* **1997**, *9* (10), 814–817.

(62) Vidil, T.; Tournilhac, F.; Musso, S.; Robisson, A.; Vidil, T.; Tournilhac, F.; Musso, S.; Robisson, A.; Leibler, L. Control of Reactions and Network Structures of Epoxy Thermosets. *Prog. Polym. Sci.* **2016**, *62*, 126–179.

(63) Innocenzi, P.; Brusatin, G.; Guglielmi, M.; Bertani, R. New Synthetic Route to (3-Glycidoxypropyl) Trimethoxysilane-Based Hybrid Organic - Inorganic Materials. *Chem. Mater.* **1999**, *11* (7), 1672–1679.

(64) Menaa, B.; Takahashi, M.; Innocenzi, P.; Yoko, T. Crystallization in Hybrid

Organic - Inorganic Materials Induced by Self-Organization in Basic Conditions. **2007**, No. 5, 1946–1953.

(65) Gabrielli, L.; Russo, L.; Poveda, A.; Jones, J. R.; Nicotra, F.; Jiménez-Barbero, J.; Cipolla, L. Epoxide Opening versus Silica Condensation during Sol-Gel Hybrid Biomaterial Synthesis. *Chem. - A Eur. J.* **2013**, *19* (24), 7856–7864.

(66) Carboni, D.; Pinna, A.; Malfatti, L.; Innocenzi, P. Smart Tailoring of the Surface Chemistry in GPTMS Hybrid Organic-Inorganic Films. *New J. Chem.* **2014**, *38* (4), 1635–1640.

(67) Baney, R. H.; Itoh, M.; Sakakibara, A.; Suzuki, T. Silsesquioxanes. **1995**, 1409–1430.

(68) Zhou, H.; Ye, Q.; Xu, J. Polyhedral Oligomeric Silsesquioxane-Based Hybrid Materials and Their Applications. *Mater. Chem. Front.* **2017**, *1* (2), 212–230.

(69) Li, Z.; Li, H.; Zhang, J.; Liu, X.; Gu, Z.; Li, Y. Ultrasmall Nanoparticle ROS Scavengers Based on Polyhedral Oligomeric Silsesquioxanes. *Chinese J. Polym. Sci. (English Ed.* **2020**, *38* (11), 1149–1156.

(70) Wang, X.; Wang, X.; Song, L.; Xing, W.; Tang, G.; Hu, W.; Hu, Y. Preparation and Thermal Stability of UV-Cured Epoxy-Based Coatings Modified with Octamercaptopropyl POSS. *Thermochim. Acta* **2013**, *568*, 130–139.

(71) Ma, Y.; He, L.; Zhao, L.; Pan, A. POSS-Based Glycidyl Methacrylate Copolymer for Transparent and Permeable Coatings. *Soft Mater.* **2016**, *14* (4), 253–263.

(72) Innocenzi, P.; Kidchob, T.; Yoko, T. Hybrid Organic-Inorganic Sol-Gel Materials Based on Epoxy-Amine Systems. *J. Sol-Gel Sci. Technol.* **2005**, *35* (3), 225–235.

(73) Pandey, S.; Mishra, S. B. Sol-Gel Derived Organic-Inorganic Hybrid Materials: Synthesis, Characterizations and Applications. *J. Sol-Gel Sci. Technol.* **2011**, *59* (1), 73–94.

(74) Li, G.; Charles, U. P. Polyhedral Oligomeric Silsesquioxane (POSS) Polymers, Copolymers, and Resin Nanocomposites. *Macromol. Contain. Met. Met. Elem. Gr. IVA Polym.* **2005**, *4* (3), 79–131.

(75) GEARY, S. A. A. L. A Theoretical Analysis of the Shape of Polarization Curves. *J. Electrochem. Soc.* **1957**.

(76) Wagner, C.; Traud, W. On the Interpretation of Corrosion Processes Through the Superposition of Electrochemical Partial Processes and on the Potential of Mixed Electrodes. **2006**, *62* (10), 843–855.

(77) Rubio, F.; Rubio, J.; Oteo, J. L. Spectroscopy Letters : An International Journal for Rapid A FT-IR Study of the Hydrolysis of Tetraethylorthosilicate. No. September 2013, 37–41.

(78) De, G.; Karmakar, B.; Ganguli, D.; Glass, C. Hydrolysis±condensation Reactions of TEOS in the Presence of Acetic Acid Leading to the Generation of Glass-like Silica Microspheres in Solution at Room Temperature. **2000**, 2289–2293.

(79) Amoriello, S.; Bianco, A.; Eusebio, L.; Gronchi, P. Evolution of Two Acid Steps Sol–Gel Phases by FTIR. *J. Sol-Gel Sci. Technol.* **2011**, *58* (1), 209–217.

(80) Monteiro, D. A.; Gozzi, G.; Luis, D.; Oliveira, O. N.; Vicente, F. S. De. Proton Conduction Mechanisms in GPTMS / TEOS-Derived Organic / Silica Hybrid Films Prepared by Sol-Gel Process. *Synth. Met.* **2020**, *267* (May), 116448. https://doi.org/10.1016/j.synthmet.2020.116448.

(81) Innocenzi, P., Figus, C., Takahashi, M., Piccinini, M., & Malfatti, L. Structural Evolution during Evaporation of a 3-Glycidoxypropyltrimethoxysilane Film Studied in Situ by Time Resolved Infrared Spectroscopy. *J. Phys. Chem.* **2011**, *115* (38), 10438–10444.

(82) Ramírez, C.; Rico, M.; Torres, A.; Barral, L.; López, J.; Montero, B. Epoxy/POSS Organic-Inorganic Hybrids: ATR-FTIR and DSC Studies. *Eur. Polym. J.* **2008**, *44* (10), 3035–3045.

(83) Muroya, M. aki. Correlation between the Formation of Silica Skeleton Structure and Fourier Transform Reflection Infrared Absorption Spectroscopy Spectra. *Colloids Surfaces A Physicochem. Eng. Asp.* **1999**, *157* (1–3), 147–155.

(84) Chou, T. H.; Chen, C. W.; Liang, C. H.; Yeh, L. H.; Qian, S. Simple Synthesis, Self-Assembly, and Cytotoxicity of Novel Dimeric Cholesterol Derivatives. *Colloids Surfaces B Biointerfaces* **2014**, *116*, 153–159.

(85) Piasek Z.; Urbanski T. The Infrared Absorption Spectrum and Structure of Urea. *Bul. L' Acad. Pol. Des Sci.* **1962**, *X* (3), 113–120.

(86) Jia, P.; Zhang, M.; Hu, L.; Feng, G.; Zhou, Y. Synthesis of Novel Caged Phosphate Esters and Their Flame Retardant Effect on Poly(Vinyl Chloride) Blends. *Chem. Lett.* **2015**, *44* (9), 1220–1222.

(87) Muruganantham, S.; Anbalagan, G.; Ramamurthy, N. Ft-Ir and Sem-Eds Comparative Analysis of Medicinal Plants , Eclipta Alba Hassk. *Rom. J. Biophys.* **2009**, *19* (4), 285–294.

(88) Bayu, A.; Nandiyanto, D.; Oktiani, R.; Ragadhita, R. Indonesian Journal of Science & Technology How to Read and Interpret FTIR Spectroscope of Organic Material. *Indones. J. Sci. Technol.* **2019**, *4* (1), 97–118.

(89) Silva, R. P. D.; Lucho, A. M. S.; Pissetti, F. L. Electrode Material Containing Graphite Incorporated to an Amino-Functionalized Polydimethylsiloxane Network for the Detection of Copper. *J. Braz. Chem. Soc.* **2018**, *29* (8), 1761–1769.

(90) Andrade, G. I.; Barbosa-Stancioli, E. F.; Mansur, A. A. P.; Vasconcelos, W. L.; Mansur, H. S. Small-Angle X-Ray Scattering and FTIR Characterization of Nanostructured Poly (Vinyl Alcohol)/Silicate Hybrids for Immunoassay Applications. *J. Mater. Sci.* **2008**, *43* (2), 450–463.

(91) Ansari, M. H.; Ahmad, M. S.; Ahmad, M. Reaction of Methyl Trans-2,3-Epoxyhexadecanoate with Urea: Synthesis of Long Chain Fatty 2-Oxazolidones. *J. Am. Oil Chem. Soc.* **1985**, *62* (12), 1659–1662.

(92) Dante, R. C.; Santamaria, D. A.; Italia, S.; Martino, V. S. Crosslinking and Thermal Stability of Thermosets Based on Novolak and Melamine. *J. Appl. Polym. Sci.* **2009**, *114* (16), 4059–4065. https://doi.org/10.1002/app.

(93) Eider, C. A.; Baptiste, M. J.; Gorka, J. Effect of Organic Precursor in Hybrid Sol – Gel Coatings for Corrosion Protection and the Application on Hot Dip Galvanised Steel. *J. Sol-Gel Sci. Technol.* **2019**, 264–283.

(94) Solids, N.; Laboratories, S. N.; Works, C. G.; York, N. Structural Evolution during the Gel to Glass Conversion. *J. Non. Cryst. Solids* **1985**, *71* (1–3), 171–185.

(95) Solids, N. Structural Evolution during the Gel to Glass Conversion. *J. Non. Cryst. Solids* **1988**, *100* (1–3), 115–141.

(96) Scherer, G. W. Sol→ Gel→ Glass: I. Gelation and Gel Structure. *J. Non. Cryst. Solids* **1985**, *70* (3), 301–322.

(97) Of, I.; Thermal, C.; Polymers, B. O. F.; Of, B.; Analysis, D. S. C. Characterization of Polymers Using Differential Scanning Calorimetry (DSC). **2017**.

(98) Mosa, J.; Durán, A.; Aparicio, M. Epoxy-Polystyrene-Silica Sol – Gel Membranes with High Proton Conductivity by Combination of Sulfonation and Tungstophosphoric Acid Doping. *J. Memb. Sci.* **2010**, *361* (1–2), 135–142.

(99) Tiringer, U.; Mušič, B.; Zimerl, D.; Šekularac, G.; Stavber, S.; Milošev, I. The Effects of Cerium Ions on the Curing , Polymerisation and Condensation of Hybrid Sol-Gel Coatings. *J. Non. Cryst. Solids* **2019**, *510*, 93–100.

(100) Ramis, X.; Cadenato, A.; Morancho, J. M.; Salla, J. M. Curing of a Thermosetting Powder Coating by Means of DMTA , TMA and DSC. *Polymer (Guildf).* **2003**, *44* (7), 2067–2079.

(101) Kang, S.; Il, S.; Rim, C.; Park, M.; Rim, S.; Kim, J. Preparation and Characterization of Epoxy Composites ® Lled with Functionalized Nanosilica Particles Obtained via Sol ± Gel Process. **2001**, *42*.

(102) L.W. KELTS, N. J. E. and S. M. M. Sol-Gel Chemistry Studied by 1H and 29Si Nuclear Magnetic Resonance. *J. Non. Cryst. Solids* **1986**, *83* (3), 353–374.

(103) Stihi, C. ATR-FTIR Spectrometry Characterisation of Polymeric Materials. *Rom. Reports Phys.* **2014**, *66* (3), 765–777.

(104) Tejedor-tejedor, M. I.; Paredes, L.; Anderson, M. A. Evaluation of ATR - FTIR Spectroscopy as an " in Situ " Tool for Following the Hydrolysis and Condensation of Alkoxysilanes under Rich H 2 O Conditions. **1998**, No. 8, 3410–3421.

(105) Lee, A. S.; Jo, Y. Y.; Jeon, H.; Choi, S. S.; Baek, K. Y.; Hwang, S. S. Mechanical Properties of Thiol-Ene UV-Curable Thermoplastic Polysilsesquioxanes. *Polymer (Guildf).* **2015**, *68*, 140–146.

(106) Larrubia, M. A.; Ramis, G.; Busca, G. An FT-IR Study of the Adsorption of Urea and Ammonia over V_2O_5–MoO_3–TiO_2 SCR Catalyst. *Appl. Catal. B Environ.* **2000**, *27* (3), L145–L151.

(107) Eshaghi, A. Transparent Hard Self-Cleaning Nano-Hybrid Coating on Polymeric Substrate. *Prog. Org. Coatings* **2019**, *128*, 120–126.

(108) Bell, J.; Nel, P.; Stuart, B. Non-Invasive Identification of Polymers in Cultural Heritage Collections: Evaluation, Optimisation and Application of Portable FTIR (ATR and External Reflectance) Spectroscopy to Three-Dimensional Polymer-Based Objects. *Herit. Sci.* **2019**, *7* (1), 1–18.

(109) Asensio, R. C.; San, M.; Moya, A.; Manuel, J.; Roja, D.; Gómez, M. Analytical Characterization of Polymers Used in Conservation and Restoration by ATR-FTIR Spectroscopy. **2009**, 2081–2096.

(110) Ram, S. Infrared Spectral Study of Molecular Vibrations in Amorphous , Nanocrystalline and AlO(OH) - H_2O Bulk Crystals. **2001**, *42*.

(111) Xu, S.; Zhao, B.; Raza, M.; Li, L.; Wang, H.; Zheng, S. Shape Memory and Self-Healing Nanocomposites with POSS−POSS Interactions and Quadruple Hydrogen Bonds. *ACS Appl. Polym. Mater.* **2020**, *2* (8), 3327–3338.

(112) Wang, L.; Deng, L.; Zhang, D.; Qian, H.; Du, C.; Li, X.; Mol, J. M. C.; Terryn, H. A. Shape Memory Composite (SMC) Self-Healing Coatings for Corrosion Protection. *Prog. Org. Coatings* **2016**, *97*, 261–268.

(113) Yang, K. H.; Ger, M. D.; Hwu, W. H.; Sung, Y.; Liu, Y. C. Study of Vanadium-Based Chemical Conversion Coating on the Corrosion Resistance of Magnesium Alloy. *Mater. Chem. Phys.* **2007**, *101* (2–3), 480–485.

(114) Souza, F. L.; Lopes, K. P.; Longo, E.; Leite, E. R. The Influence of the Film Thickness of Nanostructured α-Fe 2O3 on Water Photooxidation. *Phys. Chem. Chem. Phys.* **2009**, *11* (8), 1215–1219.

(115) Momber, A. W.; Fröck, L.; Marquardt, T. Effects of Accelerated Ageing on the Mechanical Properties of Adhesive Joints between Stainless Steel and Polymeric Top Coat Materials for Marine Applications. *Int. J. Adhes. Adhes.* **2020**, *103*, 102699.

(116) Rahimi, H.; Mozaffarinia, R.; Hojjati Najafabadi, A. Corrosion and Wear Resistance Characterization of Environmentally Friendly Sol–Gel Hybrid Nanocomposite Coating on AA508. *J. Mater. Sci. Technol.* **2013**, *29* (7), 603–608.

(117) Search, H.; Journals, C.; Contact, A.; Iopscience, M.; Address, I. P. Design of TEOS-GPTMS Sol-Gel Coatings on Rare-Earth Magnesium Alloys Employed in the Manufacture of Orthopaedic Implants. *J. Phys. Conf. Ser.* **2016**, *687* (1), 012013.

(118) Zandi-zand, R.; Ershad-langroudi, A.; Rahimi, A. Silica Based Organic – Inorganic Hybrid Nanocomposite Coatings for Corrosion Protection. **2005**, *53*, 286–291.

(119) Wu, L. Y. L.; Soutar, A. M.; Zeng, X. T. Increasing Hydrophobicity of Sol-Gel Hard Coatings by Chemical and Morphological Modifications. *Surf. Coatings Technol.* **2005**, *198* (1–3), 420–424.

(120) Davis, S. R.; Brough, A. R.; Atkinson, A. Formation of Silica/Epoxy Hybrid Network Polymers. *J. Non. Cryst. Solids* **2003**, *315* (1–2), 197–205.

(121) Prządka, D.; Marcinkowska, A.; Andrzejewska, E. POSS-Modified UV-Curable Coatings with Improved Scratch Hardness and Hydrophobicity. *Prog. Org. Coatings* **2016**, *100*, 165–172.

(122) Wang, B.; Lin, Q.; Shen, C.; Han, Y.; Tang, J.; Chen, H. Synthesis of MA POSS-PMMA as an Intraocular Lens Material with High Light Transmittance and Good Cytocompatibility. *RSC Adv.* **2014**, *4* (95), 52959–52966.

(123) Lockington, D. A.; Parlange, J. Y.; Lenkopane, M. Capillary Absorption in Porous Sheets and Surfaces Subject to Evaporation. *Transp. Porous Media* **2007**, *68* (1), 29–36.

(124) Nestor Perez. 8.1 Cathodic Protection. In *Electrochemistry and Corrosion Science*; 2016; pp 266–269.

(125) Kelly, R. G.; Scully, J. R.; Shoesmith, D. W.; Buchheit, R. G. 4.The Polarization Resistance Method for Determination of Instantaneous Corrosion Rates. In *Electrochemical Techniques in Corrosion Science and Engineering*; 2002; pp 126–127.

(126) Palanivel, V.; Huang, Y.; Ooij, W. J. Van. Effects of Addition of Corrosion Inhibitors to Silane Films on the Performance of AA2024-T3 in a 0 . 5 M NaCl Solution. *Prog. Org. Coatings* **2005**, *53*, 153–168.

(127) Metroke, T. L.; Kachurina, O.; Knobbe, E. T. Spectroscopic and Corrosion Resistance Characterization of Amine and Super Acid-Cured Hybrid Organic-Inorganic Thin Films on 2024-T3 Aluminum Alloy. *Prog. Org. Coatings* **2002**, *44* (3), 185–199.

APPENDICES

A. TMA RESULTS

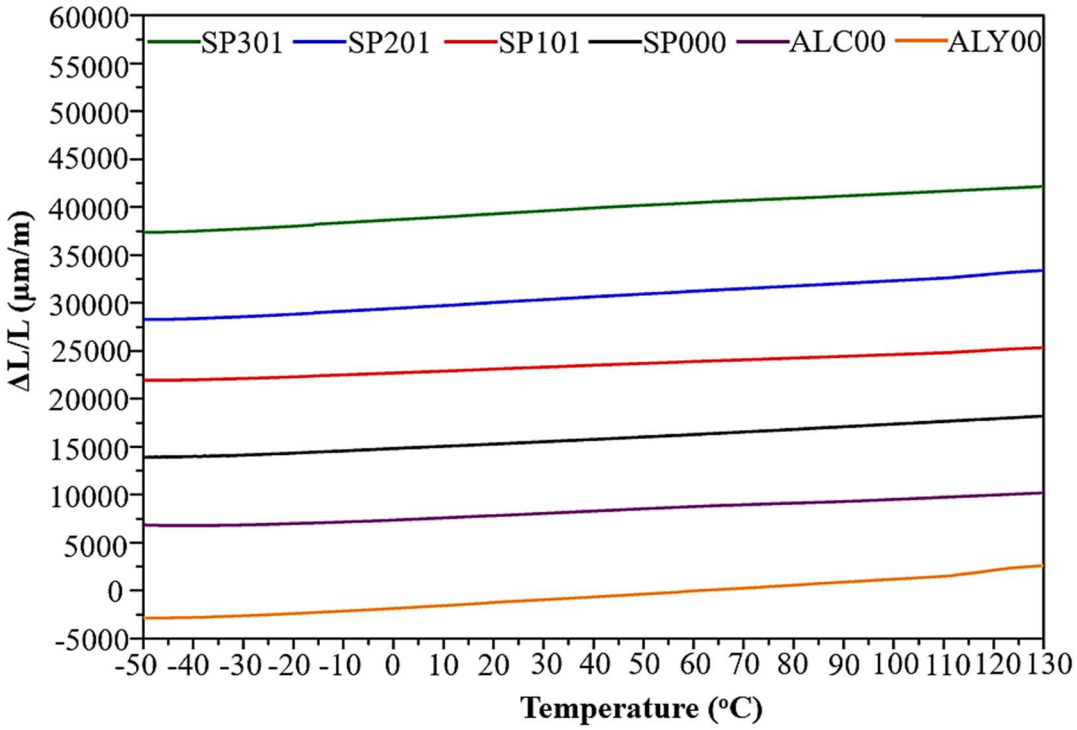

Figure A.1. TMA measurements of all coated samples with reference samples.

B. ADHESION TESTS

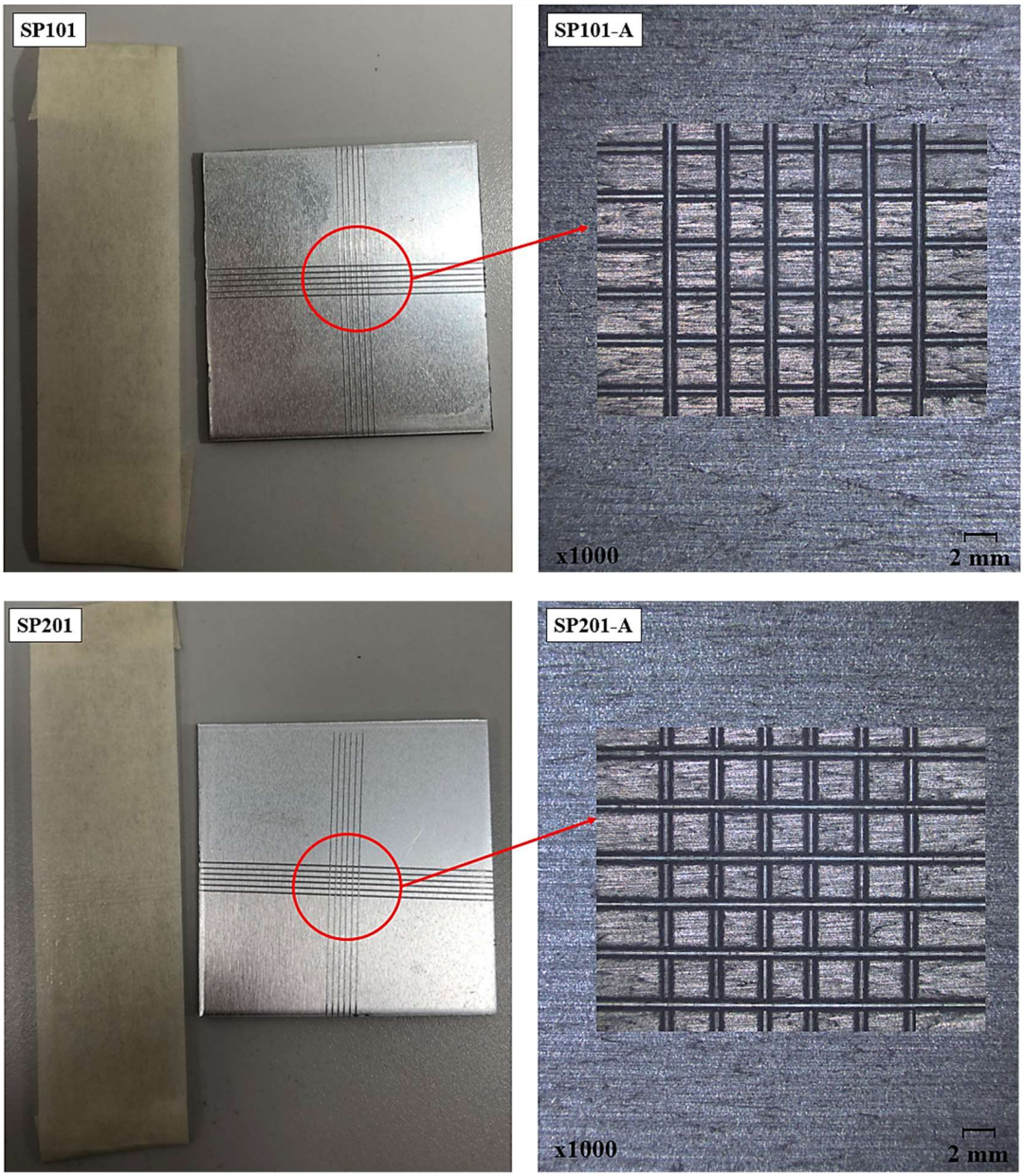

Figure B.1. Adhesion test images of SP101 and SP201.

C. TAFEL PLOTS OF ALL SAMPLES

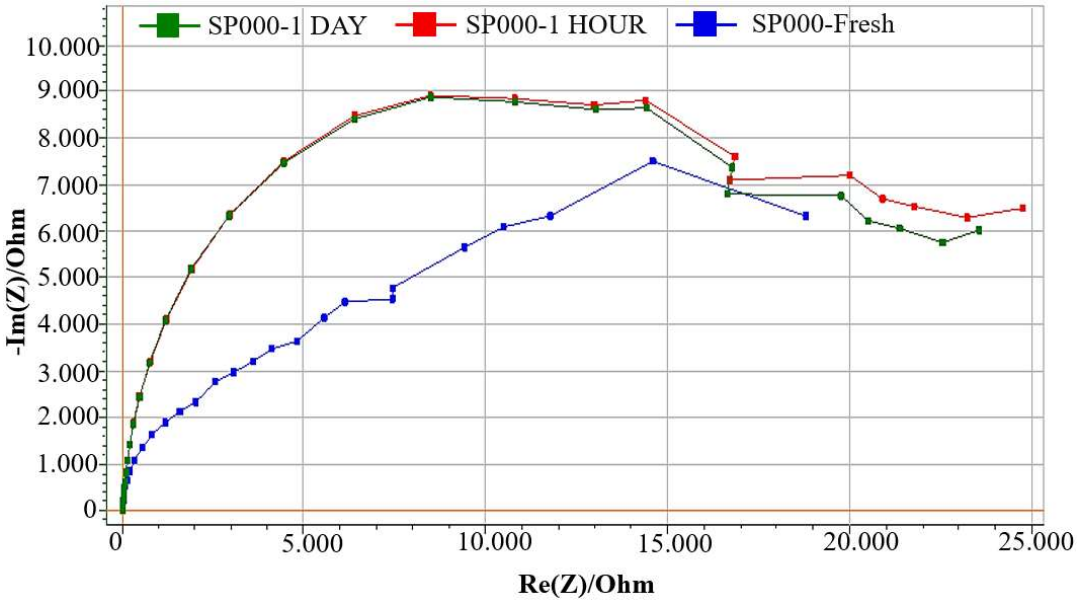

Figure C.1. Tafel plots of SP000.

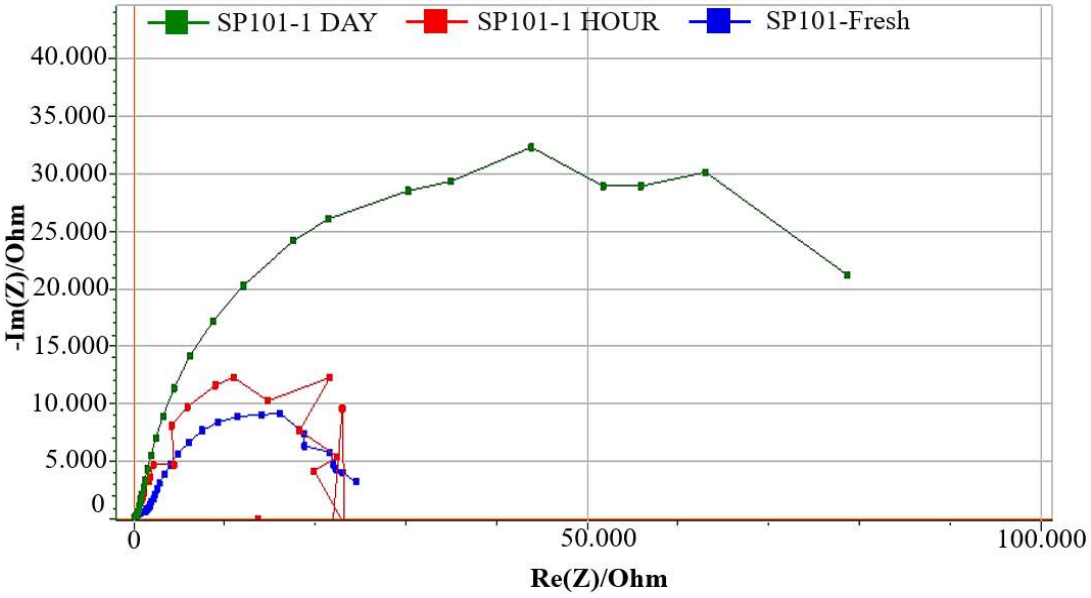

Figure C.2. Tafel plots of SP101.

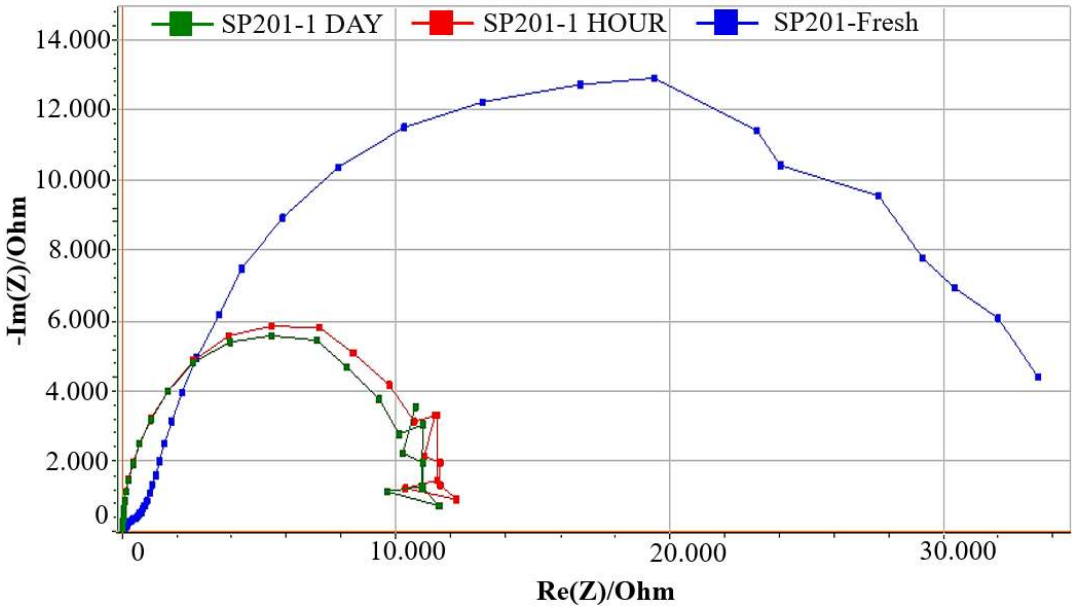

Figure C.3. Tafel plots of SP201.

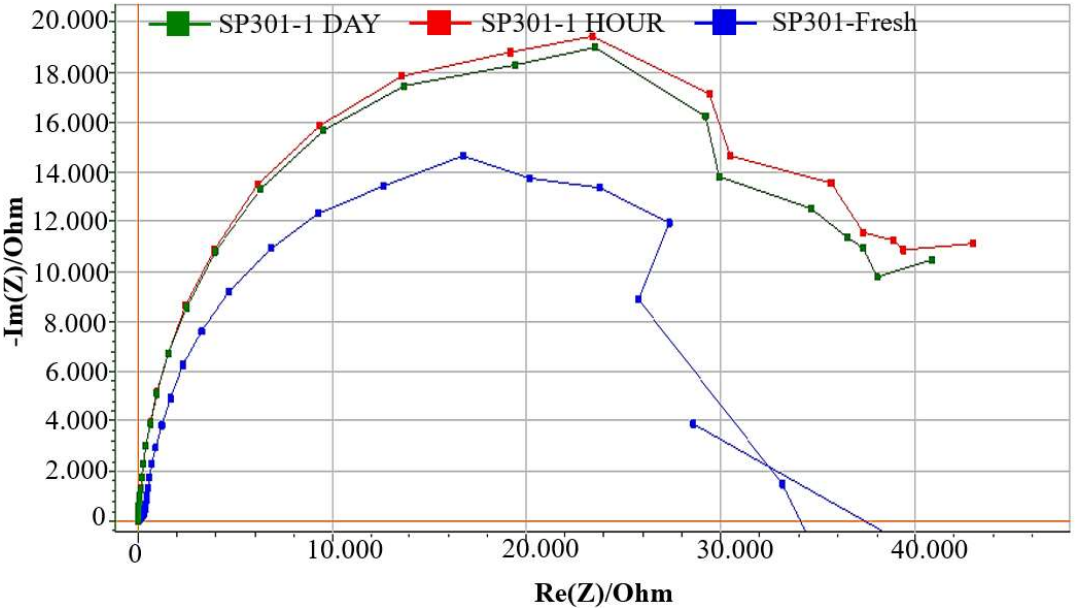

Figure C.4. Tafel plots of SP301.